JGR Earth Surface

RESEARCH ARTICLE
10.1029/2020JF005692

Climatic and Biotic Controls on Topographic Asymmetry at the Global Scale

T. Smith[1] **and B. Bookhagen**[1]

[1]Institute of Geosciences, Universität Potsdam, Potsdam-Golm, Germany

Key Points:

- Steep terrain has higher topographic asymmetry magnitudes
- Pole-facing terrain is on average steeper than equator-facing terrain
- High-elevation and low-temperature regions tend to have terrain steepened towards the equator

Supporting Information:

- Supporting Information S1

Correspondence to:
T. Smith,
tasmith@uni-potsdam.de

Citation:
Smith, T., & Bookhagen, B. (2021). Climatic and biotic controls on topographic asymmetry at the global scale. *Journal of Geophysical Research: Earth Surface*, *126*, e2020JF005692. https://doi.org/10.1029/2020JF005692

Received 22 MAY 2020
Accepted 3 DEC 2020

Author Contributions
T. Smith and B. Bookhagen designed the study, T. Smith prepared and analyzed all data, B. Bookhagen contributed to the development of the methodology. Both authors wrote the manuscript led by T. Smith.

Abstract Insolation differences play a primary role in controlling microclimate and vegetation cover, which together influence the development of topography. Topographic asymmetry (TA), or slope differences between terrain aspects, has been well documented in small-scale, field-based, and modeling studies. Here we combine a suite of environmental (e.g., vegetation, temperature, solar insolation) and topographic (e.g., elevation, drainage network) data to explore the driving mechanisms and markers of TA on a global scale. Using a novel empirical TA analysis method, we find that (1) steeper terrain has higher TA magnitudes, (2) globally, pole-facing terrain is on average steeper than equator-facing terrain, especially in mid-latitude, tectonically quiescent, and vegetated landscapes, and (3) high-elevation and low-temperature regions tend to have terrain steepened toward the equator. We further show that there are distinct differences in climate and vegetation cover across terrain aspects, and that TA is reflected in the size and form of fluvial drainage networks. Our work supports the argument that insolation asymmetries engender differences in local microclimates and vegetation on opposing terrain aspects, which broadly encourage the development of asymmetric topography across a range of lithologic, tectonic, geomorphic, and climatic settings.

1. Introduction

Topographic asymmetry (TA), or differences in the steepness of landforms facing in different directions, is a key marker of the influence of insolation on terrain morphology (Ma et al., 2013; Parsons, 1988; Pelletier et al., 2018; Poulos et al., 2012; West et al., 2014; Yetemen et al., 2010; Yetemen et al., 2015). Many previous studies have used the term "hillslope asymmetry" to describe this skewed relation between aspect and slope angles; in this study, we use the term "topographic asymmetry" as we do not distinguish between elements of hillslopes (usually described as having convex topographic curvatures) and fluvially drained parts of the landscape (generally concave topographic curvatures).

A wide range of studies have documented that asymmetries in insolation on opposing topographic aspects drive differences in surface temperature (Costard et al., 2002; Diniega et al., 2010; Kang et al., 2000; Ojha et al., 2014), freeze-thaw cycle frequency and intensity (Pelletier & Swetnam, 2017), snow cover duration (Girona-Mata et al., 2019), soil-water availability (Hoylman et al., 2018; Pelletier & Swetnam, 2017) and retention (Geroy et al., 2011; Gutiérrez-Jurado et al., 2013), water infiltration and runoff rates (Richardson et al., 2020b), vegetation ecology (Gallardo-Cruz et al., 2009; Hoylman et al., 2018; Istanbulluoglu et al., 2008; Sternberg & Shoshany, 2001), microclimate (Desta et al., 2004), plant-growth rates (Desta et al., 2004), and soil formation rates, composition, and thickness (Ben-Asher et al., 2017; Inbar et al., 2018; Johnstone, Chadwick, et al., 2017; Ma et al., 2013; Pelletier et al., 2018; West et al., 2014). It has also been suggested that underlying lithology and structure (Dohrenwend, 1978; Johnstone, Chadwick, et al., 2017; Johnstone, Finnegan et al., 2017; Kane, 1978; Richardson et al., 2020b), precipitation (Ben-Asher et al., 2017; Inbar et al., 2018), and soil type (van Breda Weaver, 1991) are important controls on the development of TA.

While region-wide estimates of TA were previously reported by Poulos et al. (2012) for the American Cordillera, and compared to a simple empirical model based on latitude, slope, annual temperature, and aridity by Pelletier et al. (2018), a consistent global analysis of TA magnitudes, directions, and environmental controls is lacking. In this research, we first estimate TA over the entire globe using consistent global digital elevation models (DEMs, 30–90 m resolution) and a novel TA metric which is sensitive to the entire slope-aspect distribution of a given region.

Previous discussion of environmental controls on the development of TA has primarily focused on the general climatic and biotic setting of a given region—for example, mean annual precipitation or dominant vegetation type. High-spatial resolution remote sensing data, however, allow for a more granular assessment of asymmetries in key environmental variables—insolation, vegetation cover, aridity, snow cover, evapotranspiration, and surface temperature—that are thought to be important controls on topography at the regional and continental scale. By comparing our calculated global TA estimates to both general climate contexts—e.g., mean annual temperature—and more specific metrics, such as the relative vegetation cover between north- and south-facing terrain, we can more deeply explore the influence of key biotic and climatic processes on the development of asymmetric topography at the global scale.

2. Data and Methods

2.1. Topographic Asymmetry Estimation

TA has previously been studied in large aspect bins (e.g., 90° or 180° bins) (e.g., Pelletier et al., 2018; Poulos et al., 2012; Yetemen et al., 2015). We expand this analysis by examining slope-aspect distributions in one-degree aspect bins to gain a deeper understanding of small-scale slope differences across terrain aspects. The distribution of slopes and aspects in a given area can be thought of as describing an ellipse, with aspect providing the angular coordinate and slope describing the radial distance from the ellipse centroid. A surface or area with equal slopes in all aspect bins—for example, on a Gaussian hill described by rotating a Gauss curve across a full 360°—will have a slope-aspect distribution which describes a perfect circle. The elliptical nature of slope-aspect distributions can be seen in real (Figure 1) and synthetic (Figure S1) landscapes. We use the 1-arc second (~30 m) global Shuttle Radar Topography Mission (SRTM) data set (JPL, 2013) and the MERIT-DEM (90 m) (Yamazaki et al., 2019) for high-resolution topography of the earth (JPL, 2013), and the MOLA MEGDR (~463m) DEM for the topography of Mars (D. Smith et al., 2003).

We capture the median slope of each one-degree aspect bin for each 0.25 × 0.25° analysis window using a minimum slope cutoff of 5°, as suggested by Poulos et al. (2012). We then fit an ellipse to each slope-aspect distribution following the least squares method of Fitzgibbon et al. (1996), which is tailored toward fitting ellipses. In our implementation, we remove the slope bins directly at the cardinal directions (45, 90, 135, etc.), as large-scale aspect distributions are known to be biased in these directions due to gridding effects and the choice of bin centers (T. Smith et al., 2019). We also perform a density filtering on the slope-aspect point distribution before ellipse fitting to eliminate outliers. In our tests, elliptical fits are robust even when several aspect bins are removed.

2.1.1. Error Bounds

In our analysis, we first remove any 0.25° boxes that do not have at least 100,000 paired slope-aspect measurements. We then use two error statistics to determine the reliability of our ellipsoidal fits—the mean absolute error (MAE), which is the average absolute distance of all slope-aspect pairs to the fitted ellipse, and the median distance (MD), which allows points inside and outside of the fitted ellipse to cancel each other out. Both statistics describe the distribution of slope-aspect pairs relative to the elliptical fit. As the sizes of the ellipses—and the spreads of the slope-aspect distributions—vary greatly throughout the study area, we normalize the fit statistics by the average ellipse radius (e.g., the mean of the semi-major and semi-minor axes). We choose only those points which have a normalized MAE or MD below 0.1, to account for the fact that a well-defined ellipse can be captured both when all points are close to the fitted ellipse line (as in Figure 1), or when slope-aspect pairs are evenly distributed above and below the fitted ellipse line. A map of fit statistics and number of contributing points to each elliptical fit can be seen in Figure S2. A full implementation of our fitting and filtering methodology can be found on Zenodo: https://doi.org/10.5281/zenodo.3839251 (T. Smith, 2020).

2.1.2. Derived Ellipse Parameters

By treating the slope-aspect distribution as an ellipse, we are able to derive several key parameters, including eccentricity, ellipse skew, and ellipse centroid. For our analysis of TA, the most relevant parameter is the ellipse centroid.

The centroid of the ellipse measures how shifted the entire slope-aspect distribution is from a perfect circle—if there was no north-south or east-west bias in terrain slope across aspects, the ellipse would be

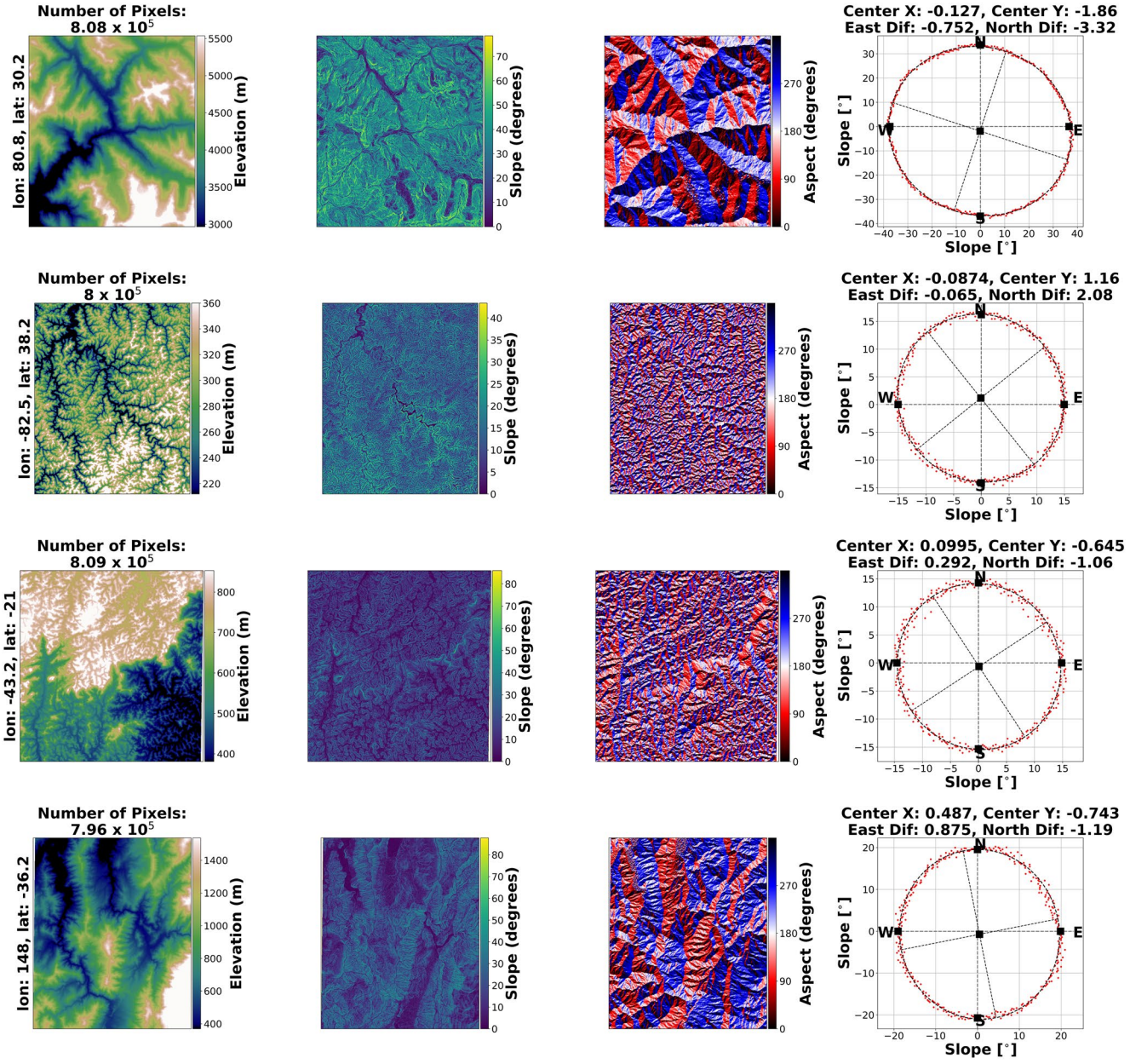

Figure 1. Elevations (first column), slopes (second column), and aspects (third column) for four selected regions, each covering one 0.25° box (~25 km across, upper left corner latitude and longitude listed on far left panel). Data are projected to local Universal Transverse Mercator (UTM) coordinates before calculation of slope and aspect. Each panel is north-up oriented. Far right column shows slope-aspect distributions and associated ellipsoid fits, with median slope of each 1° aspect bin plotted in red. Ellipsoid fit plotted in black dashed lines. Black squares show 90° binned median slopes, centered on the cardinal directions. Titles on right column compare north-south and east-west 90° binned median slope differences with x and y ellipsoid center shifts.

centered at [0,0]. When the ellipse is considered in native polar coordinates, a positive x centroid indicates that north-facing slopes are steeper than south. Similarly, a positive y centroid indicates steeper east-facing slopes. The magnitude of x-y shifts is not simply related to the absolute difference between the median slope in opposing aspects, but is instead controlled by the shape of the entire slope-aspect distribution as captured by the ellipse (Figure 1, Figure S1). Thus, we use here the ellipse centroid displacement from [0,0] as our measure of TA.

Previous work studying TA has used differences in median slope across large aspect bins to define TA. For example, Poulos et al. (2012) and Yetemen et al. (2015) compared the median slope of 90° aspect bins to

measure asymmetry, with Poulos et al. (2012) also using a logarithmic transform in their analysis of TA. When we compare our ellipse-centroid approach to a 90° binning approach, we find that the two methods do not agree on the *magnitude* of TA, but they agree on the *direction* (Figure S3). Fitting regression lines through each pair (e.g., ellipse-north vs. binned-north and ellipse-east vs. binned-east) demonstrate that elliptical asymmetry magnitudes are about half those estimated by comparing the aspect-binned medians. We attribute the differences between the two metrics to our more nuanced approach to quantifying asymmetry—our TA metric is not simply the difference in median slopes of opposing aspect quadrants, but rather represents a shift in the *entire* slope-aspect distribution, including any tilt and eccentricity of the fitted ellipse (Figure 1).

2.2. Environmental Data Preparation

2.2.1. Insolation Asymmetry Estimation

Clear-sky incident solar radiation on a surface can be calculated using models of varying complexities. In any model, the received clear-sky insolation at a surface is controlled by latitude, slope, and aspect. Here, we use both the computationally efficient method of Kumar et al. (1997) and a more complex model based on the work of Klucher (1979) to examine relative insolation differences over the entire globe (Holmgren et al., 2018).

Insolation asymmetries on slopes of different aspects can be estimated by calculating the median north-, south-, east-, and west-facing slope for each 0.25° box, using 90° aspect bins centered on each cardinal direction. These slope-aspect pairs for each 0.25° box, along with the latitude, can be used to estimate both seasonal (e.g., at each solstice) and annual clear-sky insolation on each terrain aspect, averaged over the entire 0.25° box in W/m^2. While this is not a perfect estimate of yearly insolation, it represents an efficient way to analyze insolation variability at the global scale. From these aspect-based insolation estimates, we define normalized insolation asymmetry as

$$Normalized\ Insolation\ Asymmetry = \frac{I_a - I_b}{I_a + I_b} \tag{1}$$

where I_a and I_b are the received insolation totals at aspects a and b (e.g., north and south or east and west). We choose a normalized metric to more easily compare the relative insolation received across different slope, aspect, and latitude combinations.

2.2.2. Vegetation Data and Analysis

We use three separate datasets characterizing vegetation properties: (1) Landsat-derived global vegetation continuous fields (VCF, 2000–2015, 30 m) (Sexton et al., 2013), (2) Moderate Resolution Imaging Spectroradiometer (MODIS) monthly normalized difference vegetation index (NDVI, MOD13A3, 2000–2020, 1 km) (Didan, 2015), and (3) the Global Tandem-X Forest Fraction Map (FF, 2011–2015, 50 m) (Martone et al., 2018). In combination, these three products provide a holistic view of both vegetation productivity and structure. It should be noted, however, that these vegetation datasets capture modern vegetation extents, and do not necessarily accurately represent the vegetation composition and structure of a given location over timescales relevant to the development of TA.

Two global vegetation datasets, the Landsat VCF (30 m) and Tandem-X FF (50 m), are available at comparable spatial resolutions to our elevation data. As such, we can directly compare the distribution and density of vegetation on different terrain aspects over the entire globe at 30 m resolution in a similar way to the insolation asymmetry estimated above

$$Normalized\ Vegetation\ Asymmetry = \frac{V_a - V_b}{V_a + V_b} \tag{2}$$

where V_a and V_b are the vegetation measurements at aspects a and b. For Landsat VCF, we compute a normalized ratio of the median vegetation percentage at each 90° aspect bin; for Tandem-X FF, we use the binary ratio of forested to non-forested pixels for each aspect bin. In the case of the Tandem-X data, we resample the data set to 30 m using bilinear resampling.

2.2.3. Aridity Asymmetry Estimation

Aridity has been proposed as one of the key factors which controls the magnitude of TA (Pelletier et al., 2018). Here, we use both an aridity index based on 30 arcs (~1 km) WorldCLIM data (Trabucco & Zomer, 2019; Zomer et al., 2008), as well as long-term average MODIS evapotranspiration and potential evapotranspiration (500 m, MOD16, 2001–2020) (Running et al., 2017). We capture both the median value of each 0.25° box, as well as the median value at each 90° aspect bin, centered on the cardinal directions, using the SRTM 30 m DEM resampled to 500 m (MODIS) or 1 km (WorldCLIM) to define our aspect bins. Using these binned medians, we can calculate normalized ratios of aridity, evapotranspiration and potential evapotranspiration between aspects, as in Equations 1 and 2.

2.2.4. Cold-Weather Processes

2.2.4.1. Frost-Cracking Estimates

At very high elevations and in regions dominated by exposed bedrock, frost-cracking is thought to be an important control on weathering (Anderson, 1998; Hales & Roering, 2007; Hallet et al., 1991; Matsuoka & Murton, 2008; Murton et al., 2006; Rempel et al., 2016). In particular, several authors have documented the impacts of frost cracking on catchment-averaged denudation rates (Delunel et al., 2010), slope failures (Allen et al., 2009), and headwall retreat (Scherler, 2014); Scherler (2014) noted slope differences between north- and south-facing slopes at elevations above 5,000 m. It is, unfortunately, difficult to quantify aspect control on frost-cracking directly: sufficient lithologic data are missing at the global scale and the computational intensity of frost-cracking models limits them to relatively small spatial scales.

We can, however, create a rough proxy for frost-cracking power, as segregation ice growth—the growth of ice lenses during sub-freezing periods—is thought to be a dominant erosion process in cold areas with exposed bedrock (Murton et al., 2006). Using MODIS land-surface temperature data (1 km, MOD11A1, 2001–2020) (Wan et al., 2015), we calculate the number of days within the rough "frost cracking window" of −8 to −3°C over the period 2001–2020.

2.2.4.2. Freeze-Thaw Cycle Frequency

To analyze freeze-thaw cycle frequency and temperature amplitudes, we use MODIS land-surface temperature data (1 km, MOD11A1, 2001–2020) (Wan et al., 2015) and ERA5 hourly 2-m air temperature (0.25°, 1979–2020, product t2m) (Copernicus Climate Change Service (C3S), 2019). We first define a long-term daily temperature amplitude metric from MODIS, which is the average of the difference between daytime and nighttime temperature over all high-quality data days (2001–2020). We also use the MODIS data to calculate long-term average temperature and maximum three-monthly temperature amplitude (e.g., largest difference between three-monthly temperature averages).

We define two metrics of freeze-thaw cycle frequency, one daily and one multi-day. A daily freeze-thaw cycle is defined when daytime temperature rises above 0°C and nighttime temperature sinks below −1°C (Hershfield, 1974). We define a multi-day freeze-thaw event to be when two consecutive frozen days (e.g., maximum temperature below 0°C) are followed by two consecutive thawed days (e.g., minimum temperatures above 0°C) (Sinha & Cherkauer, 2008). We apply both metrics to the ERA5 data, as we can resolve hourly differences in temperature over the entire time series. We only use the daily freeze-thaw metric with the MODIS data, as cloud contamination and other issues are likely to introduce spurious temperature results over the length of the time series. We rely instead on only days with high-quality daytime and nighttime data to calculate single-day freeze-thaw events. We find that all three metrics (e.g., MODIS daily, ERA5 daily, and ERA5 multi-day freeze-thaw cycle frequency) show similar spatial patterns, albeit with different estimated freeze-thaw cycle frequencies (Figure S4).

2.2.4.3. Snow-Cover Asymmetries

Snow cover has long been known to influence soil erosion through modifying a range of processes, including soil-water infiltration, snowmelt runoff, absorbing raindrop energy, and modifying the depth and timing of soil freezing and thawing (e.g., Edwards & Burney, 1987; Haupt, 1967; Iwata et al., 2011; Melton, 1960; Pelletier et al., 2018; Starkloff et al., 2017; West et al., 2014). Aspect, by modifying snow cover extent and duration, will also have a control on snowline altitude, which is also thought to be an important control on

erosion (Egholm et al., 2009). We quantify aspect-based snow cover asymmetries using MODIS daily snow cover estimates (500 m, MOD10A1, 2001–2020) (Hall et al., 2016) using the long-term median annual snow cover (2001–2020).

As the MODIS data are available at 500 m (snow cover) and 1 km (temperature) spatial resolution, we can examine aspect-driven differences in freeze-thaw cycling, frost cracking, and snow cover within our 0.25° analysis windows. We resample the 30 m SRTM DEM to 500 m (snow cover) and 1 km (temperature) to calculate terrain aspect for each MODIS pixel. From this, we can calculate the median freeze-thaw cycle frequency, median snow-covered area, and median number of days in the frost-cracking window over each 90° aspect bin, and use them to compute asymmetries within each 0.25° box over the entire earth, using the same normalized ratio approach as defined in Equations 1 and 2, as well as with a simple difference between the median values in each aspect bin.

2.3. Drainage Network Analysis

Our drainage analysis covers three main metrics: (1) simple drainage area statistics, (2) normalized relative drainage ratios between different aspects, and (3) log area versus log slope analysis (e.g., Kirby & Whipple, 2001; Snyder et al., 2000; Tarboton et al., 1991; Yetemen et al., 2010). We use the global MERIT-HYDRO (Yamazaki et al., 2019) data set to analyze differences in drainage area between different terrain aspects. We keep the MERIT-HYDRO data at its original 90 m spatial resolution and use the MERIT-DEM (Yamazaki et al., 2017) to calculate drainage statistics by 90° aspect bin to avoid resampling artifacts. To compare different regions of the landscape (e.g., floodplain, ridge top, and hillslope), we subdivide the landscape by drainage area into a set of logarithmic bins with varying widths ranging from two to six orders of magnitude. We only consider areas from a minimum drainage area of 0.01 km^2 to a maximum of 1,000 km^2 for this analysis.

For each drainage area subset, we capture median drainage area and slope at each 90° aspect bin. In a second step, we divide the slope and drainage area measurements for each 0.25° box into 50 log-spaced bins from their minimum to maximum drainage area, and capture the median slope of pixels within each log bin. To calculate concavity, we fit a regression to the log area versus log slope distribution, and record the slope of the regression. We only include non-zero regression slopes with a *p-value* <0.05 in our analysis. Lastly, we calculate channel steepness indices using a fixed global average concavity value (0.45), as recommended in Yetemen et al. (2010).

Following these analyses, we calculate normalized ratios between drainage areas, steepness indices, and concavities across aspect bins, as in Equations 1 and 2. It is important to note that our method differs from traditional log area versus log slope analysis in that we do not calculate concavity over individual watersheds, but rather over each entire 0.25° box.

3. Results

3.1. Theoretical Insolation Asymmetry

Both latitude and the angle of a hill relative to the sun (e.g., terrain slope and aspect) can have a large impact on insolation. For example, flat ground at the equator receives far more sunlight than flat ground near the poles (Figure S5). By the same token, a south-facing hill will receive more sunlight at a high northernly latitude than the same hill at the equator due to the impact of the solar incidence angle, assuming an idealized cloud-free world.

Using the median slope at each 90° aspect bin within each 0.25° box, we can calculate the theoretical clear-sky insolation differences between north-south and east-west aspects (Figure 2). There is a clear north-south reversal in insolation from the northern to southern hemispheres, and almost no latitude dependence in east-west insolation asymmetry (Figure 2).

3.2. North-South Asymmetry

There is a clear latitudinal north-south TA signal across the globe (Figure 3). Importantly, this signal is visible when the data are aggregated into 1° boxes as the analysis window instead of 0.25° boxes, when using a

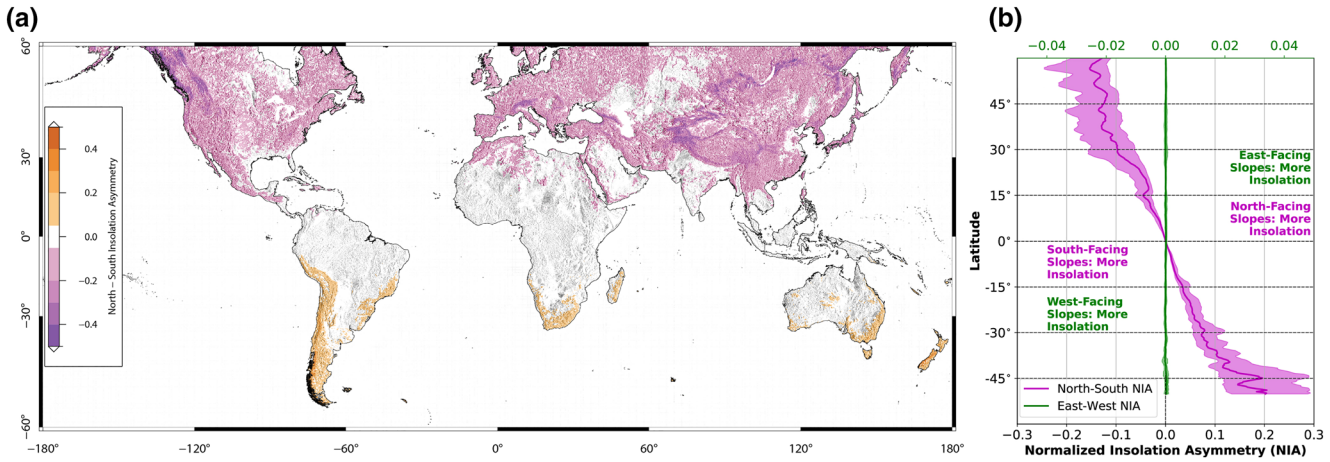

Figure 2. (a) Normalized insolation asymmetry (NIA) calculated from the difference in insolation between north- and south-facing terrain (Equation 1). South-facing terrain receives more insolation in purple regions, north-facing terrain receives more insolation in orange regions. (b) Latitudinal profiles showing average yearly insolation asymmetries between north- and south-facing (purple line) and east- and west-facing (green line) terrain. Theoretical clear-sky insolation calculated using each 0.25° box's central latitude and median slope at each 90° aspect bin with the method of Klucher (1979).

90 m DEM instead of a 30 m DEM, or when considering individual watersheds as the analysis unit instead of square boxes covering the surface of the earth (Figure S6). Global-scale TA patterns agree well with those previously proposed in the literature (Pelletier et al., 2018; Poulos et al., 2012). Fully 74% of terrain exhibiting topographic asymmetry is steeper on poleward-facing slopes.

Despite variation in regional lithologic, climatic, and tectonic settings, TA is expressed in coherent spatial patterns, particularly in the absence of tectonic activity and in stable terrain shaped over long time scales (Figure 3a). We find large regions that have consistent, uni-directional, TA—for example, both eastern Brazil (Mantiqueira Mountains) and the eastern United States (Appalachia) exhibit consistent poleward-steepened TA (Figure 3a). This pattern is repeated quasi-globally in tectonically quiescent and temperate regions, such as in Namibia, south-eastern Australia, and western Spain. Importantly, these regions are poleward-steepened, as would be expected if insolation-driven microclimatic and biotic differences are a primary driver of TA in these regions. It is also important to note that steep and high-relief terrain (e.g., the Alps, Himalaya, and Andes) has generally higher TA magnitudes.

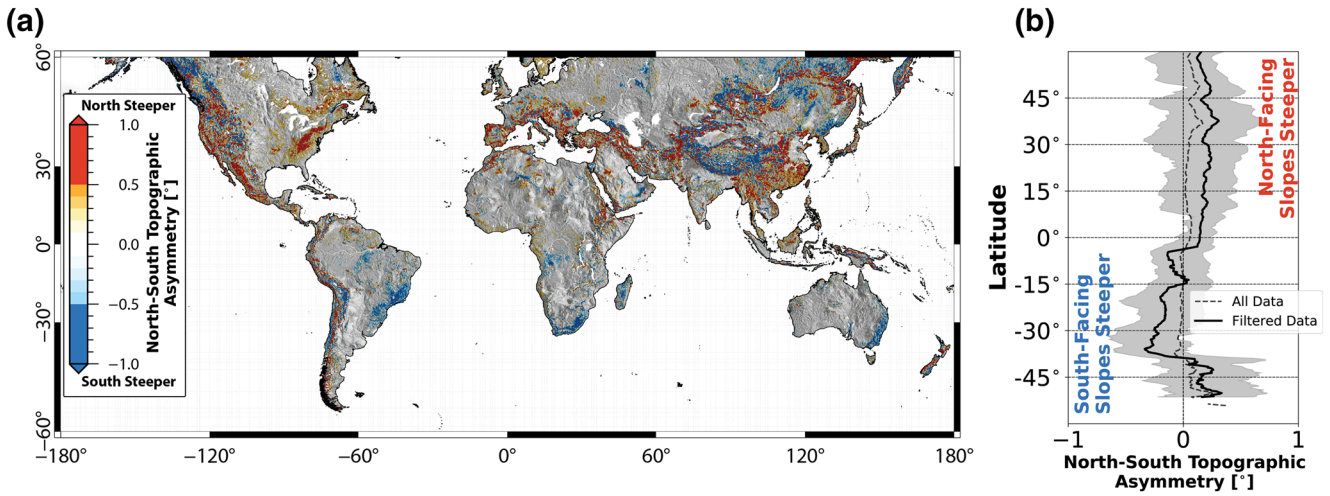

Figure 3. Global topographic asymmetry (TA) magnitudes and directions. (a) North-south TA, with very low ($|TA| < 0.1°$) values filtered out. North-facing slopes are steeper in red areas, and south-facing slopes are steeper in blue areas. (b) North-south TA aggregated by latitude, with gray area showing the interquartile range for each 0.25° latitude bin. Five-point running mean shown in black for filtered data, and shown as gray dashed line for all data (including very small TA values).

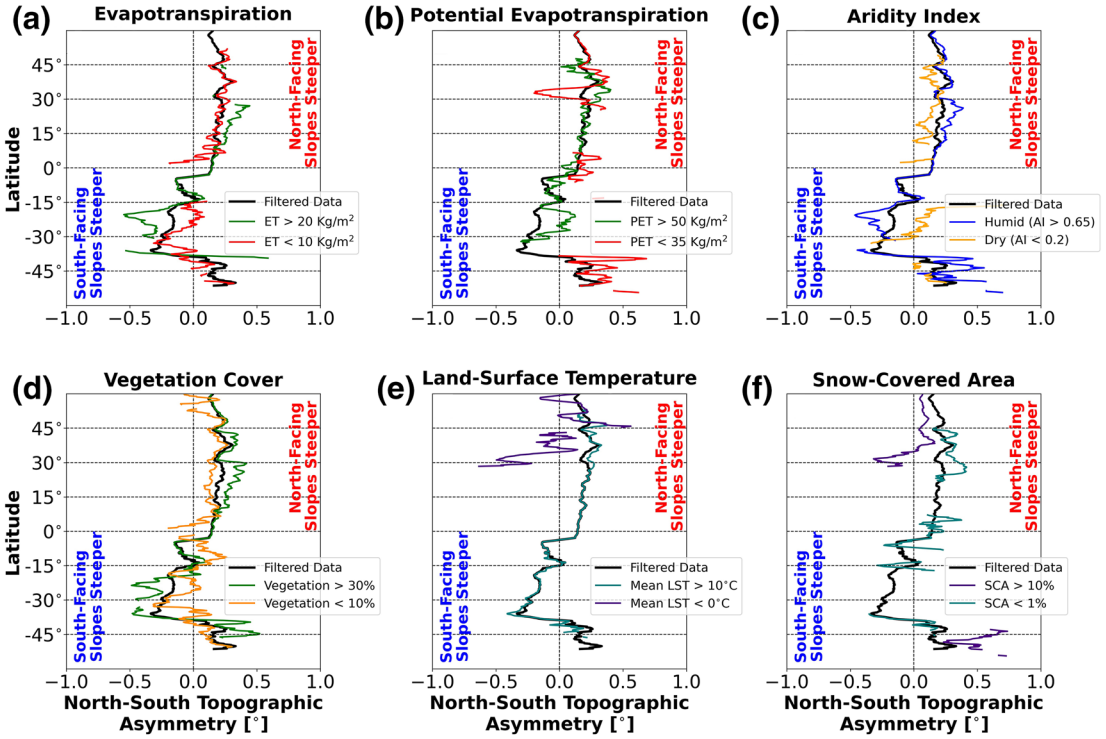

Figure 4. Latitudinal north-south topographic asymmetry (TA) patterns (black lines) divided by (a) evapotranspiration (ET), (b) potential evapotranspiration (PET), (c) aridity index (AI), (d) vegetation cover, (e) land-surface temperature (LST), and (f) snow-covered area (SCA). The magnitude and direction of each variable's impact on latitude-averaged TA is unique. High evapotranspiration, vegetation, and moisture availability encourage steepening toward the poles, low temperatures, and high snow cover encourage steepening toward the equator.

3.2.1. The Role of Climate and Vegetation

It is clear that the spatial patterns of north-south TA are complex and strongly influenced by local factors. Many relevant environmental datasets—with the notable exception of precipitation—are available at sufficiently fine spatial resolutions to resolve differences across terrain aspects. We compared a suite of environmental variables across north-south aspects and found that while each variable had some degree of latitude dependence, there was a significant difference in the magnitude of these aspect asymmetries (Figure 4).

Environmental factors can be thought of as encouraging or discouraging the processes causing poleward steepening of topography. We find that high evapotranspiration, water availability, and vegetation density all encourage poleward steepening. In contrast, low-temperature regions (mean annual temperature <0°C) and snow-covered regions tend to be less poleward steepened, or even equator steepened. While these patterns are suggestive of a process-difference between wet, temperate climates and cryospheric regions, there is a large degree of variability—TA patterns are highly local and controlled by a complex mix of environmental and climatic factors (Figure 3). It should also be noted that the magnitude of asymmetries of the environmental variables is diverse—asymmetries in aridity and potential evapotranspiration between north/south or east/west terrain are on the order of 1%–5%, while snow cover differences across aspects are on the order of 20%. The strongest aspect-dependent asymmetries among the datasets that we analyzed were present in vegetation cover.

3.2.2. Asymmetries in Vegetation

It is well-established that poleward-facing hills can store more water—given equal vegetation cover, less water evaporates on the shaded side of the hill—which has a strong impact on vegetation density and composition (Pelletier et al., 2018; Pelletier & Swetnam, 2017; Yetemen et al., 2015). There is a clear split in vegetation cover asymmetry over the equator, with vegetation cover being almost universally higher on pole-facing slopes (Figure 5).

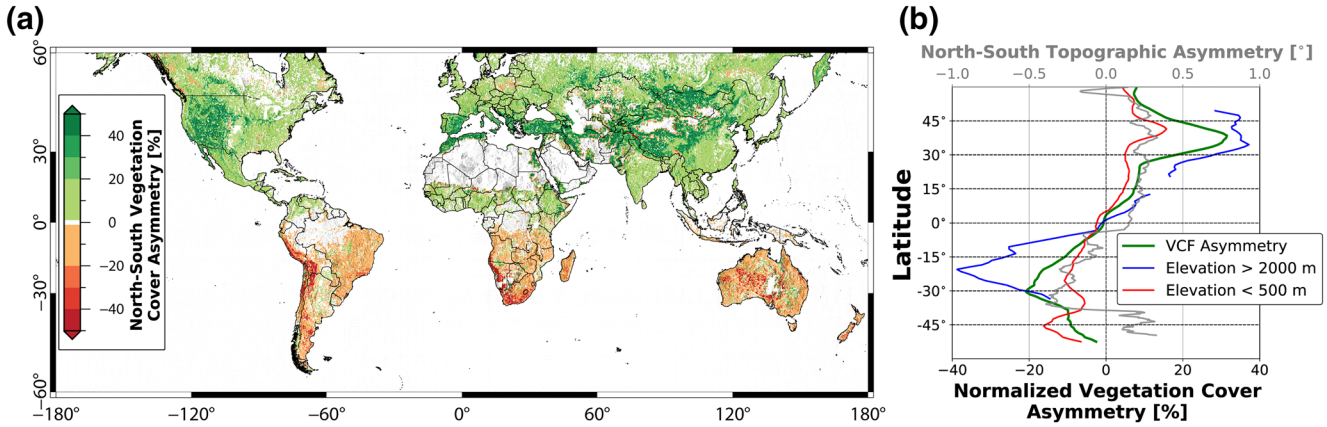

Figure 5. Vegetation cover asymmetries on opposing terrain aspects. (a) North-south normalized asymmetry in median vegetation cover percentage, based on Landsat Vegetation Continuous Fields (VCF) (Sexton et al., 2013). Green areas have higher vegetation on north-facing terrain, red areas on south-facing terrain. (b) Normalized vegetation cover asymmetry by latitude. Blue line calculated over only areas above 2000 m, red line calculated over only areas below 500 m. There is a distinct latitudinal pattern in vegetation cover where pole-facing terrain has significantly denser vegetation. This asymmetry is strengthened at higher elevations. Gray line (b, upper axis) shows north-south topographic asymmetry (TA) along latitude.

While the magnitude of vegetation asymmetry is spatially diverse, it follows a strong latitudinal pattern where the largest vegetation asymmetry is observed in the mid-latitudes (~25–45°) and at high elevations (Figure 5b). These mid-latitude regions also show significant differences in TA magnitude between vegetated and bare slopes; across most of the world, poleward steepening is enhanced when only vegetated areas are considered, and is relatively suppressed for low-vegetation regions (Figure 4d and Figure S7).

3.2.3. Asymmetries in Cryospheric Processes

To examine the asymmetric impact of frost cracking, freeze-thaw cycling, and snow cover, we use four proxies: (1) simple differences in annual average temperature and three-month temperature amplitudes (MOD11A1, Wan et al., 2015), (2) the number of days where surface temperatures are within the frost-cracking suitability window of roughly −3°C to −8°C (Delunel et al., 2010; Hales & Roering, 2007; Murton et al., 2006), (3) how often slopes are impacted by diurnal freeze-thaw cycles—defined here as when daytime temperature rises above 0°C and nighttime temperature sinks below −1°C (Hershfield, 1974), and (4) differences in annual average snow cover (MOD10A1, Hall et al., 2016).

We first find that the direction of asymmetries in three-month temperature amplitudes is controlled by both latitude—or the size of insolation differences across slope aspects—and annual average temperature (Figure 6a); annual average temperatures are generally higher on equator-facing slopes (Figure S8). Annual temperature is also important in controlling the sign of asymmetries in frost cracking and freeze-thaw cycling: cold areas will have more freeze-thaw cycling and frost-cracking on equator-facing slopes, while warmer areas will have more on pole-facing slopes (Figure 6b and Figure S9). In essence, the asymmetric action of freeze-thaw and frost-cracking processes is highly dependent on average winter temperatures—the highest asymmetries in frost-cracking and freeze-thaw cycling are found in the mid-latitudes, where temperatures move in and out of the freeze-thaw and frost-cracking windows more frequently.

Finally, snow cover has a well-defined split across the equator, with north-facing slopes having higher snow cover in the northern hemisphere, and south-facing slopes in the southern hemisphere (Figure S10). While temperature is likely the primary control on snow cover extent, differing amounts of sublimation on opposing aspects could also play a role in some areas—particularly high-elevation areas with intense insolation differences (Figure 2). However, the effects of initial snow-loading and regional precipitation patterns cannot be ruled out. While the latitudinal snow cover asymmetry profile generally follows that of TA, there is much more snow cover on south-facing slopes along the latitude band ~5–20°N. Some, but not all, of this signal comes from the south-eastern edge of the Himalaya, where snow cover is heavily dependent on the direction of moisture transport and regional topographic blocking of weather systems.

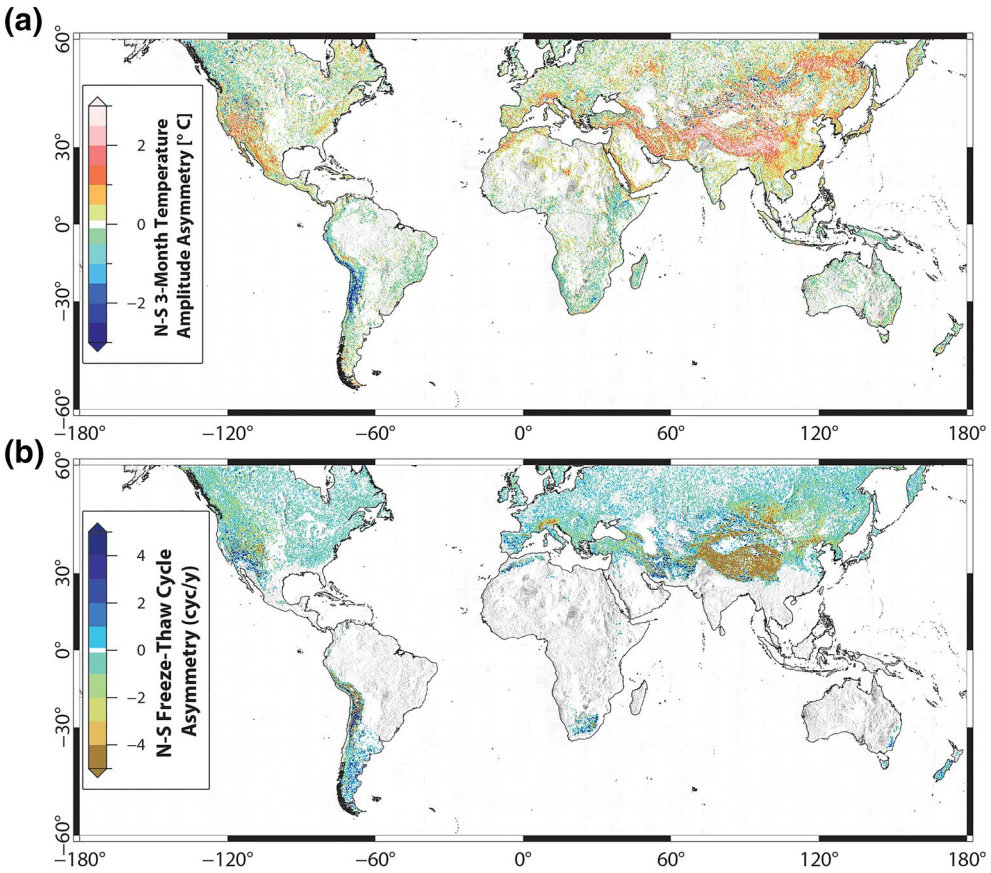

Figure 6. Direction and magnitude of cryospheric process asymmetries. (a) Annual three-month temperature amplitude and (b) freeze-thaw cycle frequency asymmetries between north and south-facing slopes. These processes are both latitude and temperature dependent—there is not a clear north-south split over the equator, but rather multiple sign reversals across latitudes.

3.3. East-West Asymmetry

Differences in topography, vegetation, and climate are also visible between east- and west-facing terrain; the magnitude of east-west TA is significantly less than that of north-south TA (Figures 3 and 7). Given that insolation differences between east- and west-facing terrain are negligible (Figure 2), a different interpretation of the causes of east-west TA is required.

The ambient air temperature during peak sunlight hours, relative persistence of morning dew periods, timing of maximal cloud cover, and dominant wind transport direction are often different on east- and west-facing slopes (e.g., Evans, 1977; Evans & Cox, 2005; Parsons, 1988; Pelletier & Swetnam, 2017; B. Smith, 1978). However, these mechanisms have not been comprehensively studied with regards to the development or maintenance of TA. While we find that west-facing hills are generally steeper across the Earth (Figure 7), this asymmetry signal is weaker than the north-south TA by a factor of two, and only 56% of asymmetric terrain shows steeper west-facing terrain.

As with north-south asymmetry, there is a clear global aspect dependence in vegetation density (Figures 7c and 7d). While there are a few regions where east-facing slopes have higher vegetation density—most notably along the east coast of the United States and in parts of north-central Asia—there are no latitudes where average vegetation density is higher on east-facing slopes. The effect is even more pronounced at high elevations, particularly in the Andes, where elevations above 2000 m have more than 60% more vegetation on west-facing slopes. The American West, Middle East, and parts of southern Africa also exhibit extreme east-west vegetation density differences (Figure 7c).

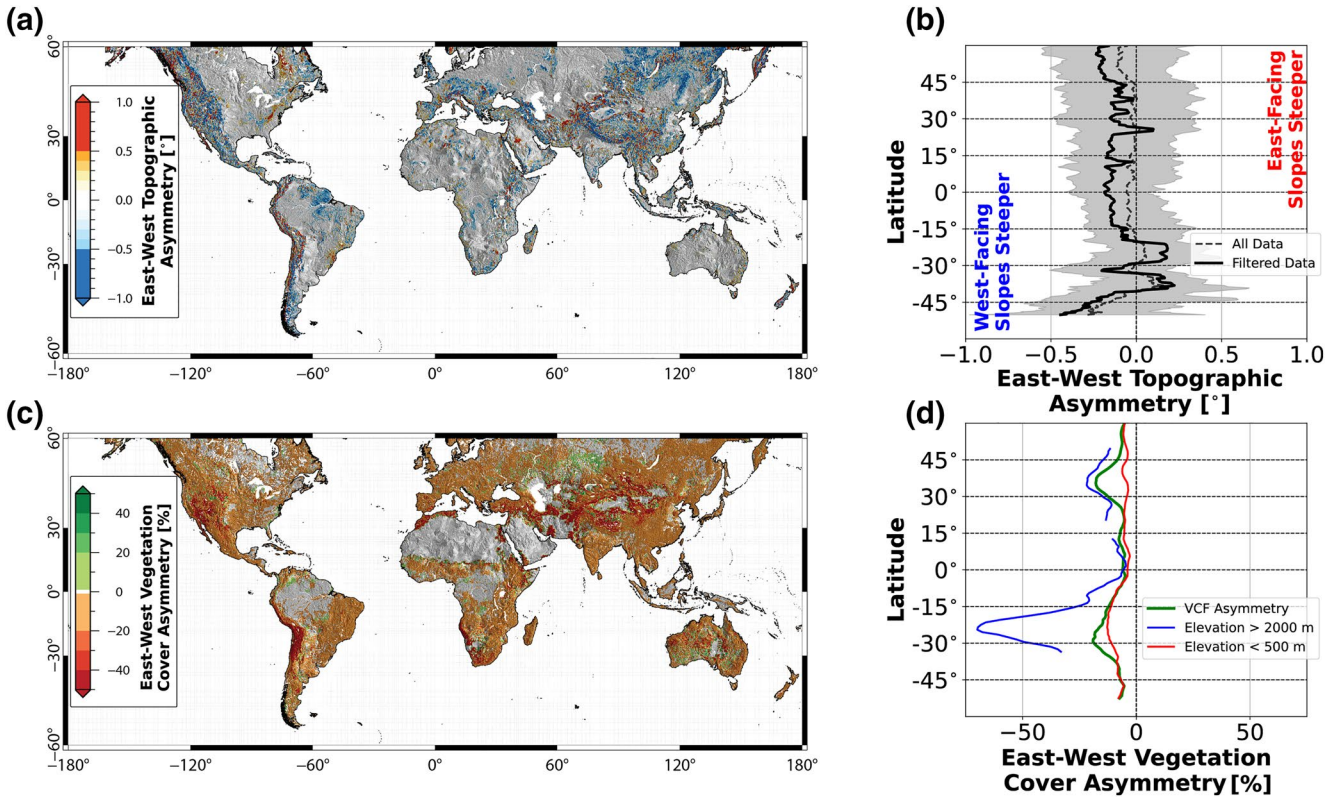

Figure 7. East-west (a), (b) topographic and (c), and (d) vegetation cover (VCF) asymmetries. Panels (b) and (d) show latitudinal profiles. (a) East-west topographic asymmetry (TA), with very low ($|TA| < 0.1°$) values filtered out. East-facing slopes are steeper in red areas, and west-facing slopes are steeper in blue areas. (b) Gray area shows the inter-quartile range for each 0.25° latitude bin. Five-point running mean shown in black for filtered data, and shown as gray dashed line for all data (including very small TA values). (c) Green areas have higher vegetation on east-facing terrain, red areas on west-facing terrain. (d) Normalized vegetation cover asymmetry by latitude. Blue line calculated over only areas above 2000 m, red line calculated over only areas below 500 m.

3.4. Preferred Topographic Asymmetry Orientation

It is clear from Figures 3 and 7 that topography is not simply asymmetric in one direction. Indeed, several studies have noted that the greatest TA occurs between northeast- and southwest-facing terrain in the northern hemisphere (e.g., Anderson et al., 2013; Kidron et al., 2016; Pelletier & Swetnam, 2017; B. Smith, 1978). Using our elliptical definition of topographic asymmetry, a combined east-west and north-south asymmetry vector can be derived between the fitted ellipse centroid and the point [0,0]. We capture both the magnitude and direction of that vector, as well as the ratio of north-south to east-west absolute TA magnitudes, to estimate the relative impact of north-south and east-west asymmetry over the globe (Figure 8).

Absolute TA magnitudes are highest in high-slope and high-relief areas, such as the Andes, Himalaya, Alps, and Cascades (Figure 8a). Ratios between north-south and east-west TA show that north-south TA is dominant in those same mountainous regions, while east-west TA is generally larger in less complex terrain (Figure 8b). There are, however, notable exceptions to this rule; East Africa and the Andes show large regions of higher east-west TA magnitudes.

When we consider the combined north-south and east-west vector, it is clear that the preferred direction of TA is highly local, particularly in complex tectonically active regions such as the Himalaya and Andes (Figure 8c). Even in tectonically quiet regions, there exists large variability. For example, while the main Appalachian region is primarily north-steepened, north-east steepening is also fairly common. Similarly, southern Africa is primarily south-steepened, with south-west steepening also occurring. South-western Australia is fairly equally south, south-east, and south-west steepened. There is no clear global pattern pointing toward a preferred north-east or south-west steepening as opposed to north- or south-steepening, but rather significant local variability in preferred steepening direction.

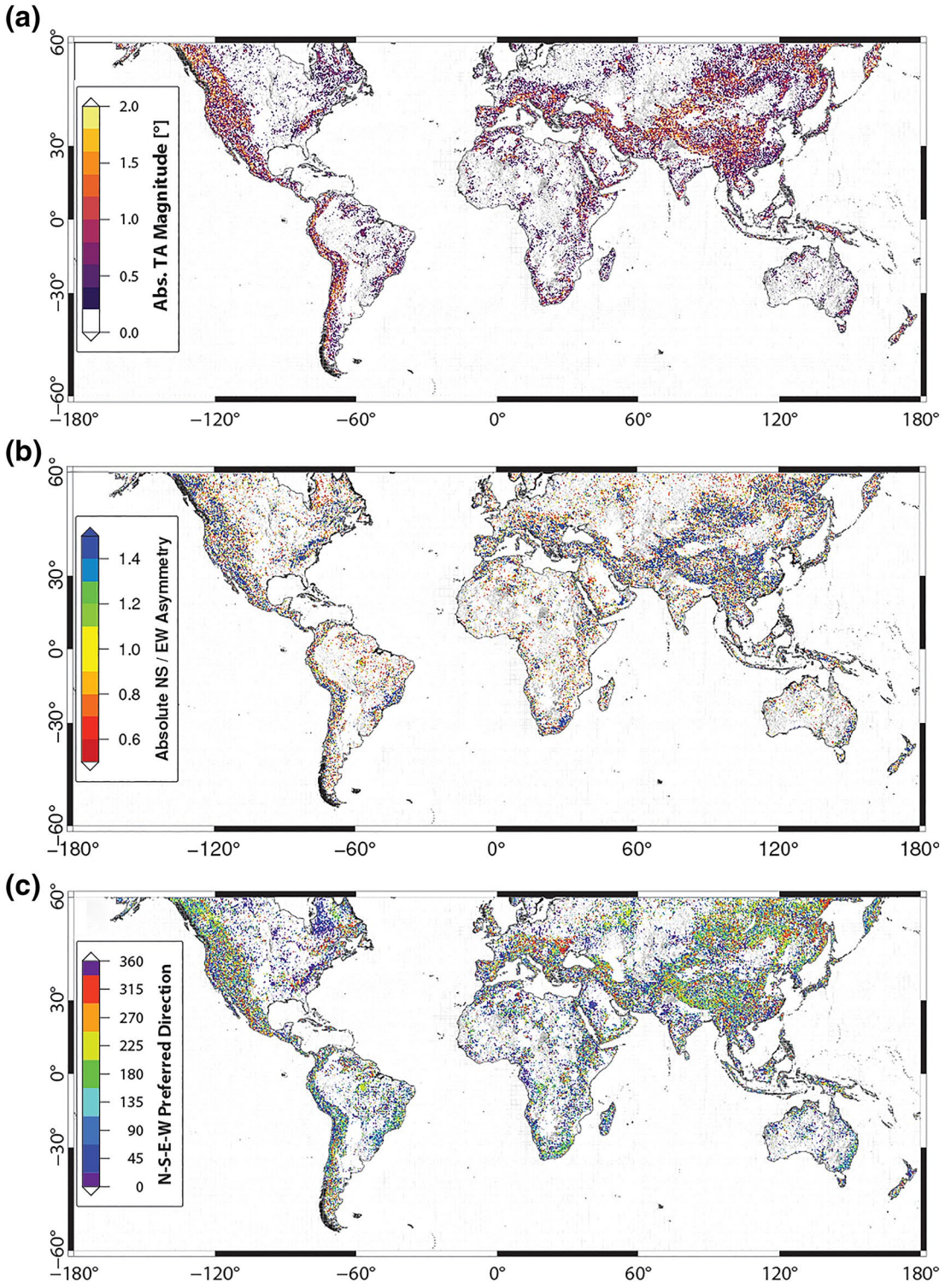

Figure 8. (a) Absolute topographic asymmetry (TA) magnitude, (b) ratio of north-south to east-west TA magnitude, and (c) preferred asymmetry orientation, defined using both the north-south and east-west TA magnitudes. High magnitude TA is generally confined to steep and high-relief areas. North-south TA is larger than east-west in most locations, with the notable exceptions of low-elevation areas and some mountain ranges such as the Andes. Preferred asymmetry directions are highly local.

4. Discussion

Aridity, vegetation, temperature, and insolation have been identified as key factors controlling global-scale TA (Ben-Asher et al., 2017; Inbar et al., 2018; Pelletier et al., 2018; Poulos et al., 2012; Richardson et al., 2019; Yetemen et al., 2015). Indeed, there are clear changes in the relationship between TA and latitude across different vegetation and temperature regimes (Figure 4). Insolation strongly influences land-surface temperature, which in turn impacts vegetation by controlling soil-water content, and cryospheric processes by driving both diurnal and seasonal temperature cycles, controlling frost cracking intensity, and modifying snow cover. It is clear from the global data that vegetation generally enhances poleward-steepening of terrain (Figure 4d), and that low temperatures enhance equator-steepening (Figure 4e). However, the influence of vegetation and temperature is relatively subtle, and is confounded by the complexity and diversity of tectonic and erosional regimes.

4.1. Vegetation Influences on Topographic Asymmetry

Vegetation cover has been linked to erosion rates and hillslope stability through a range of mechanisms (e.g., Acosta et al., 2015; Ben-Asher et al., 2017; Boer & Puigdefábregas, 2005; Dietrich & Perron, 2006; Marston, 2010; Olen et al., 2016). It plays a key role in soil respiration and formation—root systems help water infiltrate into soil mantles, which can increase soil formation rates, bioturbation, and the magnitude of diffusional processes (Ben-Asher et al., 2017; Giorgi, 1988; Johnstone, Finnegan, et al., 2017; Johnstone & Hilley, 2015; Lebedeva & Brantley, 2013; Marston, 2010; McGuire et al., 2014; Pelletier et al., 2011; Pelletier et al., 2018; Richardson et al., 2019, 2020b; Yetemen et al., 2010). Increasing vegetation cover will generally diminish soil loss rates (Acosta et al., 2015; Boer & Puigdefábregas, 2005), increase soil cohesion (Ben-Asher et al., 2017), and reduce runoff (Richardson et al., 2020b). As pole-facing terrain generally has higher vegetation cover (Figure 5), increased downslope soil transport efficiency on equator-facing slopes will relatively steepen pole-facing terrain (West et al., 2014).

4.1.1. Insolation Controls on Vegetation

We find a striking insolation control on vegetation asymmetry, where vegetation asymmetry is maximum around ±0.2, or a ∼20% difference in insolation (Figure 9). At very low insolation asymmetries—for example, around the equator—and at very high insolation asymmetries—for example, at very high latitudes or steep slopes—vegetation asymmetries are fairly low. However, these end members represent two very different processes—low vegetation asymmetries in humid and tropical areas do not behave the same way as highly seasonal high-latitude vegetation. Medium insolation asymmetries associated with mid-latitudes generate the highest vegetation asymmetries, though not always the highest topographic asymmetries.

While most regions conform to the typical pattern of vegetation asymmetry encouraging TA, there are a few important outliers (Figure 9). Blue regions with high normalized vegetation asymmetry and red regions with low normalized vegetation asymmetry represent areas which are in opposition to the general trend of pole-facing slope steepening. In particular, the grouping of red points (TA values ∼1–1.5) at negative vegetation asymmetry and positive insolation asymmetry (high latitude, southern hemisphere) indicates that vegetation cover is not the only factor controlling the direction and magnitude of TA in some regions.

4.1.2. The Impact of Aridity

Previous work has identified aridity as a key control on the development of TA (Pelletier et al., 2018). It is well known that moisture availability controls vegetation density and structure, and hence soil-creep and other erosion processes (Richardson et al., 2019); in poorly vegetated areas, it can also impact differential soil moisture and water infiltration (Churchill, 1981). It is clear from Figures 5 and 7 that terrain aspect plays an important role in controlling vegetation density. When the latitudinal vegetation asymmetry profiles are split into wet (aridity index >0.65) and dry (aridity index <0.2) regions following the classification scheme of Middleton and Thomas (1997), the importance of aridity in controlling the magnitude of vegetation asymmetry can be seen (Figure 10).

Water-limited and high-elevation environments—for example, in the High Andes, the Australian Outback, and the Tibetan Plateau—show much larger than average vegetation asymmetries (Figures 5 and 7). We posit that the differences in insolation between north-south aspects, and the timing of peak insolation on

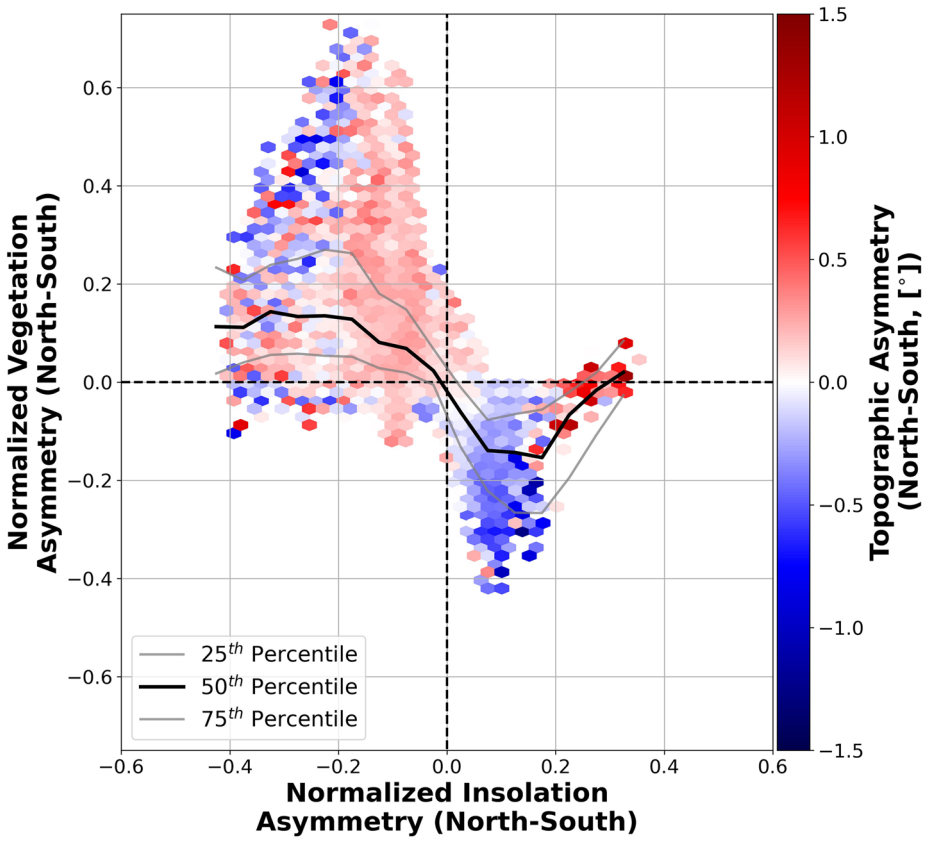

Figure 9. North-south relationship between normalized insolation and vegetation asymmetries (Equations 1 and 2). Equally sized x and y bins (n = 55,55) colored by median north-south topographic asymmetry (TA). Median (black) and interquartile-range (gray) lines plotted for all data. Positive (negative) TA indicates areas that have steeper north- (south-) facing slopes. Positive (negative) vegetation asymmetries indicate more vegetation on north (south) facing terrain. Vegetation asymmetries do not scale linearly with insolation asymmetry, but rather reach a maxima around ~20% difference in insolation between slopes. The red (positive TA) region with positive insolation asymmetry (north-slopes receive more insolation) and low vegetation asymmetry indicates that vegetation is not the only controlling factor in the development and maintenance of TA.

east-west aspects, generate soil moisture differences between opposing aspects that are particularly important in already water-stressed environments. Our data suggest that those soil-moisture differences have a large impact on vegetation cover, particularly in water-limited environments where vegetation growth is strongly influenced by moisture availability (Figures 5 and 7).

Based on the finding that vegetation cover enhances TA (Figure 4), we propose that aridity is not a primary control on the development of TA in most of the world, but rather plays a second-order role in modifying vegetation growth and structure, which in turn enhances or decreases TA. While the development of TA in some regions (e.g., hyperarid parts of the Andes) may be influenced by wetting/drying of the soil or other weathering processes in the absence of vegetation, these processes are unlikely to be dominant in most of the world.

4.2. Low-Temperature Environments

There are many regions which are not steepened toward the poles, such as above 50°N and in high-elevation mountain ranges throughout the northern hemisphere (Figure 3). It has been suggested that equator-steepening in regions north of ~50°N in the Columbia Mountains of northwestern Canada is due to the impacts of glacial erosion, particularly during the last glacial maximum (Poulos et al., 2012). Other glaciated and high-elevation regions have also shown similar equator-steepened topography (e.g., Melton, 1960; Naylor & Gabet, 2007; Parsons, 1988; Pierce & Colman, 1986). While glacial erosion certainly impacts TA, there are other potential drivers of spatially extensive equator-steepening at high elevations and latitudes.

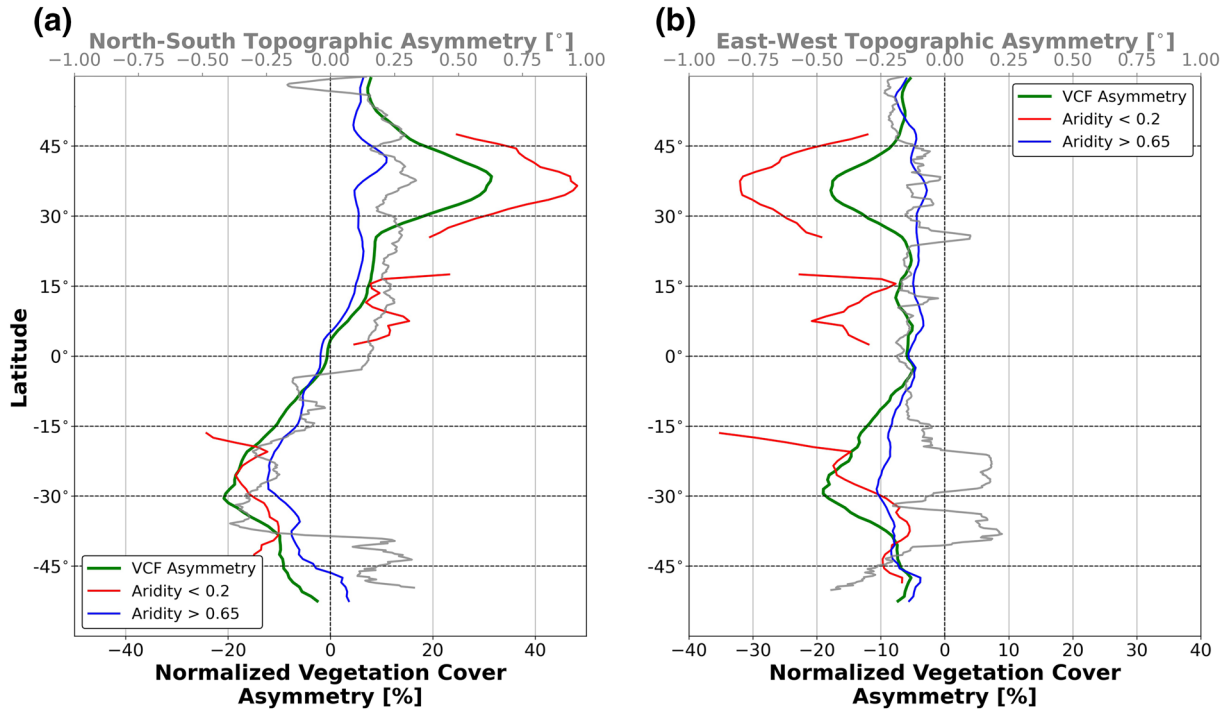

Figure 10. (a) North-south and (b) east-west normalized vegetation cover asymmetry (Sexton et al., 2013) (green lines, Equation 2) subdivided into wet (aridity index >0.65, blue lines) and dry (aridity index <0.2, red lines) regions (Middleton & Thomas, 1997). Dry regions have enhanced vegetation asymmetry, and wet regions have relatively suppressed vegetation asymmetry.

Insolation driven temperature differences across aspects can modify the intensity and frequency of many key erosion processes; without insolation freeing liquid water, many processes are weakened or cease to function. Seasonality, and the frequency and magnitude of both seasonal and diurnal freeze-thaw cycles, will also drive differences in bedrock shattering, surface erosion, and soil formation processes (Anderson et al., 2013; Matsuoka, 1990). In some environments, freeze-thaw cycles will also induce solifluction, which can lead to rapid erosion of soil mantles (Crampton, 1977; Marshall et al., 2015). However, equator-steepening of slopes is a relatively localized phenomenon (Figure 3) and is generally confined to high-elevation and cold regions, such as the Alps, Caucasus, and Himalaya.

4.2.1. Regional Impacts of Cryospheric Processes

The southern Himalaya have been subjected to strong prevailing winds and more or less continuous monsoonal rainfall for the past 10 Ma (Clift et al., 2014; Gupta et al., 2015). This, all else being equal, should lead to higher erosion on those south-facing slopes and commensurate drainage divide migration northward—hence steepening north-facing slopes. However, the Himalaya remain one of the most strongly south-steepened regions on Earth (Figures 3 and 11a), indicating that for that set of lithologies and prevailing moisture transport directions, fluvial erosion and divide migration is likely not the key TA-forming process (Clark et al., 2004; Whipple et al., 2017). While long-term temperature data are unfortunately not available at high (e.g., 30 m) spatial resolution, we can make rough estimates of cryospheric process asymmetry at the kilometer scale using MODIS land-surface temperature data (Wan et al., 2015) (Figure 11).

We find that many equator-facing slopes in High Mountain Asia experience more frequent freeze-thaw cycles—defined as days where the daytime temperature rises above 0°C and nighttime temperature sinks below −1°C—than pole-facing slopes (Figure 11c and Figure S9). This freeze-thaw cycle asymmetry is generally confined to high-elevation regions and regions with high daily temperature amplitudes (Figure 11b). These high-elevation regions also experience larger seasonal temperature differences, and more asymmetric frost-cracking (Figure 6).

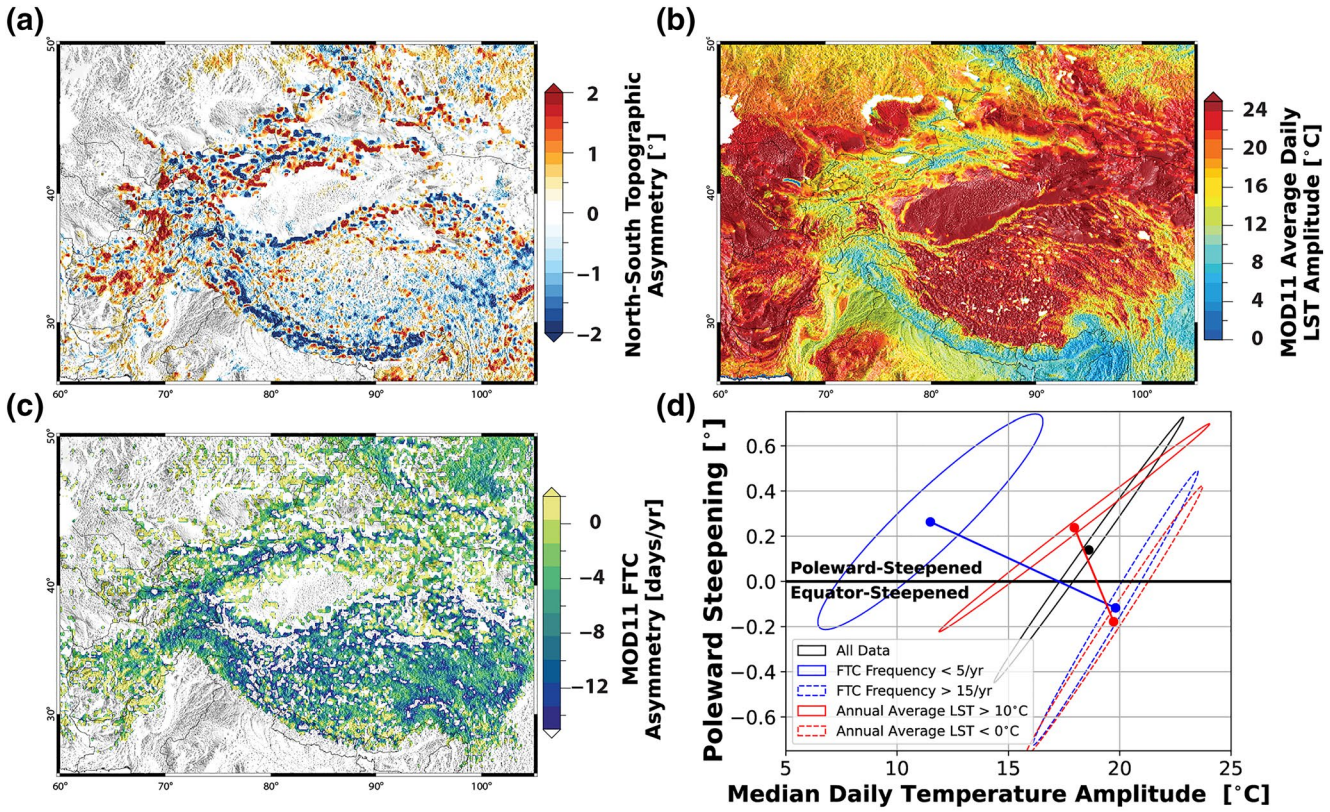

Figure 11. (a) North-south TA, (b) average daily land-surface temperature amplitude from MODIS MOD11 (Wan et al., 2015), and (c) north-south freeze-thaw cycle (FTC) asymmetry over High Mountain Asia (HMA). FTC asymmetry is calculated as the difference in long-term average freeze-thaw cycle frequency between north- and south-facing slopes. Large areas of equator-steepening overlap with cold regions with high freeze-thaw cycle frequency. (d) Median daily temperature amplitude compared with degree of poleward steepening over HMA. Ellipses show one standard deviation confidence bounds for different subsets of the data. Cold regions or regions with more frequent freeze-thaw cycles (dashed ellipses) are more equator-steepened than warm areas without frequent freeze-thaw cycles (solid ellipses).

Strongly equator-steepened slopes are also observed in other regions with frequent freeze-thaw cycles; for example, the Southern Andes, European Alps, and American Rockies all have regions of equator-steepened terrain concentrated where freeze-thaw cycle frequencies are high and annual mean temperatures are low (Figures 11–14). Importantly, equator-steepening occurs in both regions with intense tectonic uplift (e.g., the Himalaya, Andes, New Zealand) and more stable terrain (north-eastern Eurasia, the Caucuses) where active tectonics are unlikely to play a large role in driving TA, and other asymmetry-forming processes are likely dominant. It is important to note, however, that the magnitude of cryospheric processes—most notably but not exclusively glacier processes—is also controlled by moisture availability. For example, glacial occurrence on the southern Himalayan front is mostly controlled by temperature (Amidon et al., 2013), while glacier occurrence in the arid Puna Plateau in the south-central Andes is controlled by precipitation (Haselton et al., 2002).

4.2.2. Extreme Cold: The Case of Mars

To test whether equator-steepening is prevalent in an extremely cold and vegetation-free end-member case, we have extended our analysis to the surface of Mars. Our results confirm those of Kreslavsky and Head (2003), which showed general equator-steepening of slopes on Mars—particularly in the band running from 40 to 50° latitude in both hemispheres (Figure S15). Occasional insolation-driven temperature increases on pole-facing slopes during periods of high obliquity can cause differences in surface ice distribution, lead to relatively more frequent freeze-thaw cycles, and allow for the sporadic presence and deeper penetration of liquid water, as well as occasional overland flow (e.g., Chevrier & Rivera-Valentin, 2012; Costard et al., 2002; Diniega et al., 2010; Head et al., 2003; Kreslavsky & Head, 2003; Ojha et al., 2014; Page, 2007; Rubanenko et al., 2019), which has led to shallower pole-facing slopes. However, the latitude-TA

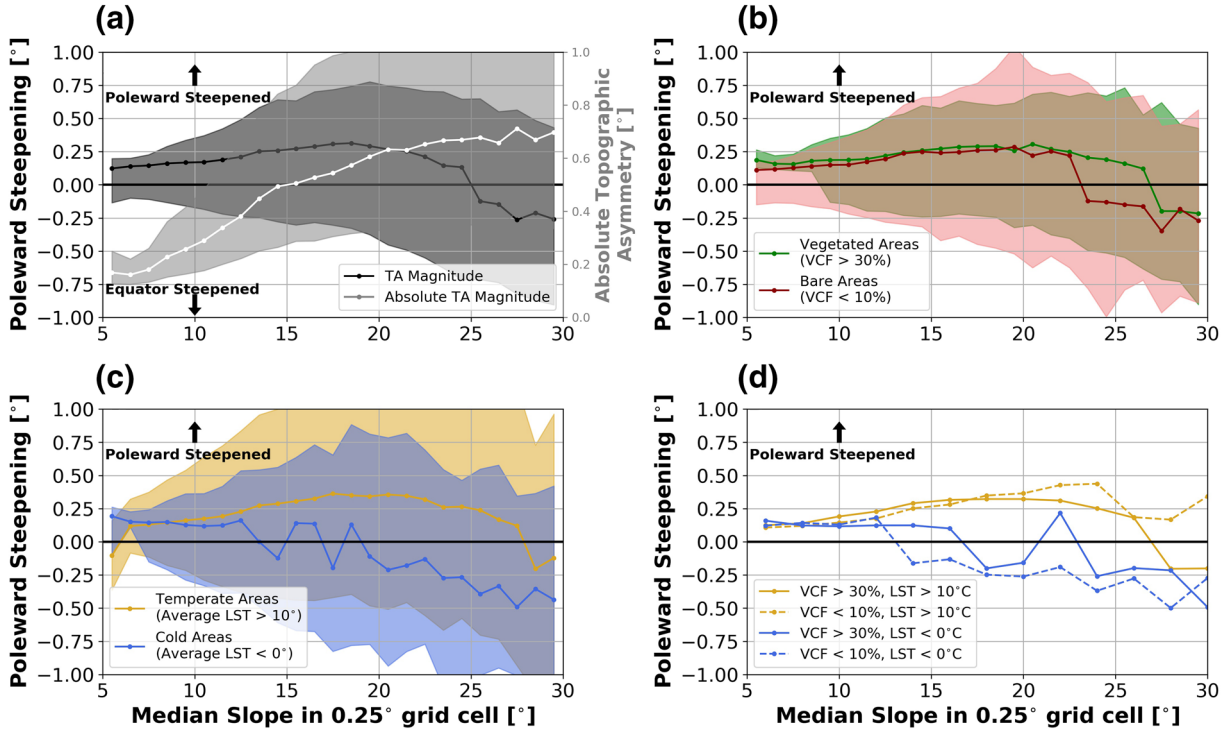

Figure 12. (a) Median terrain slope compared to degree of poleward steepening (black line) and absolute topographic asymmetry (TA) magnitude (white line). TA magnitude generally scales with slope. (b) Median degree of poleward steepening in vegetated (green) and bare (red) areas. (c) Median degree of poleward steepening in temperate (orange) and cold (blue) areas. (d) Median degree of poleward steepening split by both mean annual temperature (LST, orange: temperate, blue: cold) and vegetation cover (VCF, solid lines: vegetated, dashed lines: bare). Shaded areas show 25th–75th percentile confidence intervals. Mean annual temperature is a stronger predictor of equator-steepening than vegetation cover.

relationship on Mars is much weaker than on Earth (Figure S15). Lower data density, slower soil formation rates, the frequency of impact craters, past large-scale glaciations, lower gravitational acceleration, the shifting axial tilt of the poles, and large-scale loss of atmosphere could all contribute to the relatively subtle TA signal. A more in-depth study with higher resolution data would be required to better constrain TA magnitudes on Mars.

4.3. Morphologic and Environmental Controls on Topographic Asymmetry Magnitude

Terrain which is north-steepened or south-steepened can also be thought of as being poleward- or equator-steepened—essentially the sign of TA in the southern hemisphere can be reversed. By redefining terrain as either poleward- or equator-steepened, we can align the asymmetry estimates from the northern and southern hemispheres into a single metric, and use this to compare asymmetry over the entire globe to environmental and topographic metrics. We can also simplify TA further by calculating its absolute magnitude.

We find that the magnitude of TA is partially controlled by the steepness of the terrain; the absolute magnitude of TA—either pole- or equator-steepened—generally scales with terrain slope (Figure 12a). The degree of poleward steepening of landscapes increases with median terrain slope until ~18°; after ~25° of slope, topography tends toward equator steepening (Figure 12a). We posit that this shift represents a change in regime from continuously soil-mantled regions to steep, mountainous terrain with only patches of soil cover, as proposed for slopes above ~30° by Heimsath et al. (2012). The transition to discontinuous soil-cover or exposed bedrock would likely engender a process transition toward landsliding in steeper terrain (Heimsath et al., 2001; Heimsath et al., 2012), which could be partially responsible for the reversal of the asymmetry signal seen at high slopes. It is also possible, however, that environmental factors—such as the preponderance of low-temperatures and sparsity of vegetation cover in many high-relief regions—also play a role. Above ~30° of slope, data density is too low to effectively compare median terrain slope and TA at the scale of our 0.25° boxes.

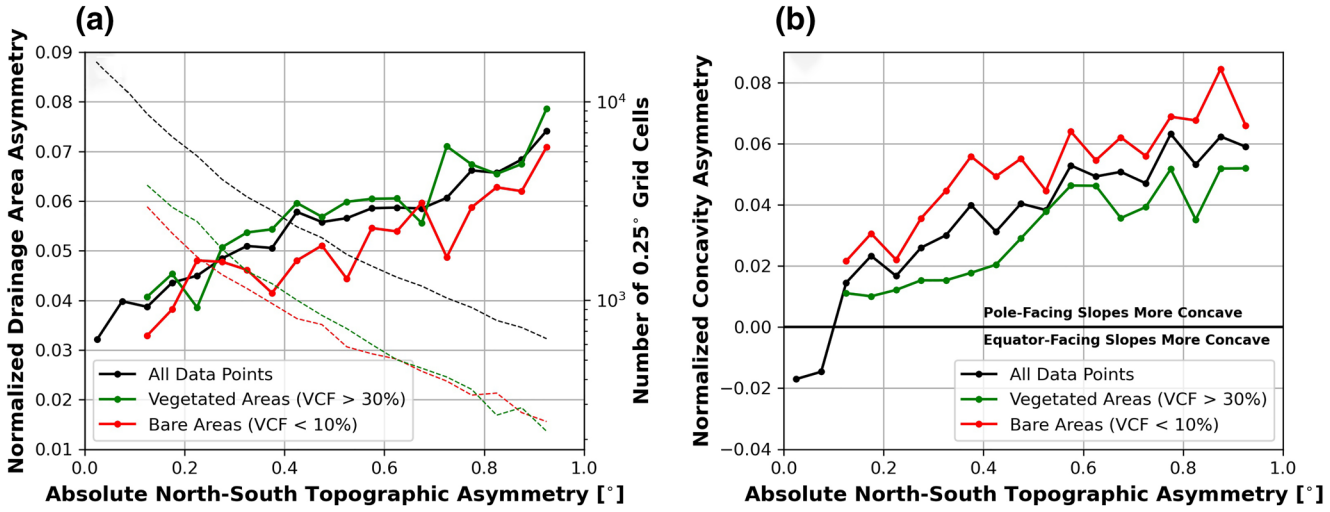

Figure 13. Absolute north-south topographic asymmetry (TA) magnitude compared to (a) drainage area and (b) concavity asymmetries. Black lines show median of all data points, green of only vegetated areas, and red of non-vegetated areas. Dashed lines on (a) show relative data density between vegetation subsets. In general, bare areas have less drainage area asymmetry but more concavity asymmetry than vegetated areas. The magnitudes of relative drainage area and concavity asymmetries scale with TA.

When the relationship between terrain slope and TA is split between vegetated and non-vegetated areas (Figure 12b), there is not a strong impact on the direction or magnitude of TA until ~15° of slope. Above this threshold, vegetated terrain remains poleward-steepened as median slope increases, while bare terrain tends toward equator-steepening; this shift is, however, slight. A similar relationship can be found when terrain is divided into temperate and low-temperature subsets—cold regions tend toward higher absolute TA magnitudes and more equator-steepened topography (Figure 12c). To further disentangle the relative impacts of vegetation and temperature on TA, we have subdivided the data by both vegetation and temperature simultaneously (Figure 12d). It is clear that while both temperature and vegetation cover play a role in controlling the direction and magnitude of TA, temperature is a stronger factor in driving the equator-steepening of terrain.

4.4. Asymmetries in Drainage Networks

Differences in terrain slope (Figures 3 and 12) and vegetation (Figure 5) with aspect should lead to changes in the structure of drainage networks (e.g., drainage network density, concavity, and steepness) (Dunne, 1980; Istanbulluoglu & Bras, 2005; Johnstone, Finnegan, et al., 2017; McGuire et al., 2014; Perron et al., 2009; Richardson et al., 2020b; Yetemen et al., 2010). For simplicity, we focus here on two subdivisions of the landscape: 0.1–100 km^2 (generally drainage areas at lower hillslope sections and floodplains) and 0.01–1 km^2 (drainage areas at upper hillslope sections and ridges). Latitudinal patterns in drainage area and concavity asymmetry (Figure S16) mirror those seen in TA and vegetation asymmetry (Figures 4d and 5b).

Asymmetrically steepened terrain has relatively higher drainage area asymmetries (Figure 13a). In general, neighboring terrain is exposed to similar conditions (e.g., lithology, rainfall, and base elevation level which they drain to). For pole-facing terrain to have larger drainage areas on relatively steeper slopes, a difference in topographic form is required. We find that differences in drainage network concavity mirror large-scale latitudinal patterns in TA, vegetation asymmetry, and drainage area asymmetry (Figure S16). One possible explanation for this phenomenon is the significantly higher vegetation cover on pole-facing terrain, especially in arid and mountainous regions (Figure 5). Vegetation cover has been linked to slope stability and concavity, as well as river network form (e.g., Chen et al., 2019; Collins & Bras, 2010; Ielpi & Lapôtre, 2020; Istanbulluoglu & Bras, 2005; Yetemen et al., 2010); Chen et al. (2019) found a systematic trend toward less concave river profiles in more arid environments. Higher vegetation cover could lead to steeper hillslope angles and ultimately steeper river channels, which could explain the higher concavities and drainage areas on pole-facing terrain.

Indeed, if we subset the drainage area and concavity asymmetry measurements by vegetation cover, we see differences in their scaling magnitude versus TA (Figure 13). Bare terrain has more asymmetric concavities than vegetated terrain across all TA magnitudes. Bare terrain also tends to support smaller drainage area asymmetries; this relationship remains nearly constant across TA magnitudes (Figure 13a). Similarly, cold areas have higher drainage area asymmetries but smaller concavity asymmetries than temperate areas (Figure S17). By extending this analysis of drainage networks to include channel steepness asymmetries (e.g., Kirby & Whipple, 2001; Snyder et al., 2000; Tarboton et al., 1991; Yetemen et al., 2010), we find that asymmetries in hillslope concavity and drainage network density are reflected downstream in the fluvial network—pole-facing channels are generally steeper (Figure S16).

It is important to note, however, that determining whether differences in the fluvial network are transmitted to the hillslopes (e.g., differences in drainage area on opposing slopes lead to asymmetric topography), or asymmetries in hillslopes lead to changes in drainage networks (e.g., asymmetric terrain modifies drainage network form), is difficult. While our data suggest that drainage network asymmetries mirror TA, constraining the direction and magnitude of the diversity of vegetation, climatic, fluvial, and lithologic processes—and the complex feedbacks they engender—would require further in-depth analysis.

4.5. Implications for Landscape Evolution

A range of mechanisms explaining TA patterns have been suggested in the literature across different eco-hydrological zones and spatial scales. Yetemen et al. (2015) suggest based on landscape evolution modeling that poleward steepening is driven by increased erosion on equator-facing slopes, which have less vegetation cover and thus higher transport efficiency. Inbar et al. (2018) propose that pole-facing hillslopes are steeper due to denser vegetation which allows for steeper slopes as a product of soil cohesion. Pelletier et al. (2018) argue that TA is driven by differences in downslope transport, where equator-facing slopes have higher drainage densities which drives drainage divide migration. West et al. (2014) posit that TA arises from differences in transport efficiency between hills with divergent soil thicknesses. McGuire et al. (2014) and Rasmussen et al. (2017) suggest that vegetation differences between poleward- and equator-facing hillslopes lead to higher bioturbation and soil-water retention capacity, and thus higher rates of colluvial transport. While there is a wide-ranging consensus that pole-facing slopes on Earth are generally steeper, the process controls are still debated.

We argue that in vegetated landscapes, higher vegetation covers on pole-facing terrain encourages resistance to erosion by overland flow and diffusion. Hence, equator-facing slopes exhibit higher erosion rates where—all else being equal—diffusive and advective processes are more effective and generally result in shallower slopes. This is supported by the strong north-south vegetation density asymmetry observed at a global scale (Figure 5), and by the relatively stronger north-south TA signal observed in wet areas (Figure 4), where vegetation asymmetries are higher. Mid-latitude TA is relatively higher due to insolation controls on the magnitude of vegetation asymmetries (Figure 9); lower TA at high latitudes and around the equator partially reflects relatively low vegetation asymmetries.

In high elevation and cold environments, a different set of erosion processes play a role in the development of TA. Periglacial processes can encourage equator-steepening of topography via intense erosion on pole-facing slopes and headwall retreat (Melton, 1960; Naylor & Gabet, 2007; Pierce & Colman, 1986). Pole-facing terrain in extremely cold environments remains frozen and stable for more of the year – indeed, in permafrost landscapes, the differences in temperature amplitude between pole- and equator-facing slopes can be quite large (Figure 6). Freeze-thaw cycling also acts more forcefully on equator-facing slopes, primarily through enhancing solifluction (Marshall et al., 2015), slumping (Crampton, 1977; Parsons, 1988), and modifying soil-water penetration and overland flow (Edwards & Burney, 1987; West et al., 2014). In high-relief and tectonically active environments, hillslope-transport processes will thus remove more material on equator-facing slopes. Where material transport is high, for example in steep river valleys, this material may not lead to gentler slopes at higher erosion rates. Even where material transport is low, slumping and mass movement could lead to terrain with steep upper sections and shallow lower sections rather than a more gradual and smooth hillslope form as is typical in mid-latitude regions. As we discount slopes under 5° from our analysis, we may preferentially remove the signals associated with low-slope debris deposits in some areas.

While TA in high elevation and cold environments is likely also impacted by vegetation differences (e.g., warmer, equator-facing terrain may maintain higher vegetation cover), we do not see this in vegetation asymmetry at the global scale (Figures 5 and 9). The lack of a convincing vegetation asymmetry signal at high elevations and latitudes, however, does not preclude the influence of temperature-limited vegetation suitability on the development of TA; the snapshot modern vegetation data used in this study does not capture the influence of past vegetation regimes on the development of topography—particularly in regions where climate has shifted dramatically over millennial timescales. It remains likely that differences in vegetation productivity and composition at high elevations and latitudes also play a role in the development of equator-steepened terrain (Pelletier et al., 2018).

4.6. Data Limitations, Caveats, and Future Outlook

While our global analysis of topographic form covers many key processes and variables, there remain some important limitations of this work that should be mentioned. Our analyses of the controls on the development of TA rely primarily on empirical data, and are hence limited to what we can effectively measure on a global scale. Among the many variables we cannot include in this analysis, three stand out as likely to play large roles in the development of local and global topographic asymmetries: (1) lithology, soil, and geologic structure; (2) precipitation and moisture transport directions; and (3) tectonic activity. It is important to emphasize that while global-scale trends can explain much of the TA signal, the processes driving the development of TA can also be highly regional or local (Figure 3).

Underlying geologic structure and lithology, as well as soil type, depth, and formation rates, are known to influence the magnitude of TA by controlling erosion patterns and resultant landscape form (Dohrenwend, 1978; Johnstone, Chadwick, et al., 2017; Johnstone, Finnegan, et al., 2017; Kane, 1978; Richardson et al., 2020a, 2020b; West et al., 2014). Many regions—particularly those formed through compressional tectonics—have underlying bedrock forms that can enhance or suppress the expression of TA at the regional or even continental scale. The issue of lithology and soil is perhaps even more important: erosion rates are heavily influenced by the durability and cohesion of the exposed surficial or bedrock material (e.g., Heimsath et al., 2012); soil depth also exerts a strong control on erosion rates (West et al., 2014). Unfortunately, global lithologic, soil, and fault maps of sufficient spatial resolution simply do not exist to incorporate into our analysis.

Prevailing moisture transport directions and precipitation asymmetries can play a large role in controlling rainfall, vegetation, snowfall, glaciation, and freeze-thaw processes—particularly in water-limited environments (Evans, 1977; Haselton et al., 2002; Olen et al., 2016). Assessing asymmetries in precipitation between different terrain aspects is, however, not currently possible at the global scale; the spatial resolution of precipitation data is at least an order of magnitude too coarse to resolve small-scale differences across topography. Similarly, without better constraints on uplift rates and directions, quantifying the role of active tectonics in the development of TA remains difficult.

Finally, the issue of process scale should also be considered—our analysis of TA and other environmental asymmetries takes place over fairly large regions: 0.25° (~25 km) boxes. Many studies which have related topography to certain process controls have focused on much smaller landscapes with very localized constraints on climate and geology. Our results and analysis are relevant at a broad scale and across varied lithologies; the processes that we propose to drive topographic asymmetry will not necessarily create the same landforms at finer spatial scales and in regions with variable rock strength, consolidation, and soil cohesion. It is also important to note that we consider 30 m gridded elevation data, which will resolve different features than those studied with high-resolution lidar data.

While we do not propose a new process-based landscape evolution model, we would recommend, based on the empirical evidence presented here, that (1) insolation, (2) vegetation, and (3) temperature asymmetries between opposing aspects be included in future modeling efforts. Modeling efforts should also be able to reproduce the limitations on freeze-thaw processes and vegetation asymmetries induced by insolation (Figure 9), aridity (Figure 10), and temperature (Figure 6). Finally, any proposed model should be able to

reproduce our finding that steeper slopes have more asymmetric topography (Figure 12), perhaps through an aspect-slope-dependent diffusion law or a coupled vegetation cover-diffusion model.

5. Conclusions

Based on the empirical evidence presented in this study, we identify insolation as driving asymmetries in microclimate on opposing terrain aspects. Regional differences in vegetation, temperature, climate, lithology, and tectonic activity modify key landscape processes so that the same insolation asymmetry can lead to very different landscapes. We first quantify global topographic asymmetry patterns and find that steeper terrain has higher topographic asymmetry magnitudes. We further find that in temperate environments, the poleward steepening of terrain can be primarily explained by vegetation cover differences on opposing aspects. In cold environments, asymmetries in freeze-thaw cycling, frost cracking, and snow cover help suppress the poleward steepening of terrain; periglacial and other cryospheric processes can also help encourage equator-steepening of terrain. Topographic asymmetry patterns are, however, highly sensitive to local geology, climate, and vegetation. Finally, we find that asymmetries in topographic form are reflected in the size and shape of fluvial drainage networks. New global estimates of asymmetries in insolation, vegetation cover, cryospheric processes, and drainage network form presented in this study support our analysis, and underline the importance of insolation as a key control on climate, biota, and erosion processes. Large-scale global patterns of asymmetric vegetation cover, temperature fluctuations, and landscape form are modified by local microclimate, lithology, and tectonics, leading to the complex expression of topographic asymmetry across the globe.

Competing Financial Interests

The authors declare no competing financial interests.

Data Availability Statement

All data sets used in this study are publicly available (Didan, 2015; Dimiceli et al., 2015; Hall et al., 2016; JPL, 2013; Running et al., 2017; Wan et al., 2015; Yamazaki et al., 2017, 2019; Sexton et al., 2013; D. Smith et al., 2003; Zomer et al., 2008). The authors have uploaded a large tabular data set including our aspect-oriented estimates of means in each variable described in this study to Zenodo: https://doi.org/10.5281/zenodo.4019109. The initial codes used to process the topographic data have been released at https://doi.org/10.5281/zenodo.3839251 (T. Smith, 2020). Ongoing updates will be available at https://github.com/UP-RS-ESP/HillslopeAsymmetry.

Acknowledgments
The State of Brandenburg (Germany) through the Ministry of Science and Education and the NEXUS project supported T. Smith for part of this study (grant to B. Bookhagen.). The authors also acknowledge support from the BMBF ORYCS project. The authors thank Stephanie Olen and Ben Purinton for comments on an earlier version of the manuscript. The authors would also like to acknowledge the detailed and comprehensive reviews of Jon Pelletier, Amy East, Noah Finnegan, Sam Johnstone, Erkan Istanbulluoglu, Amanda Schmidt, and four anonymous reviewers.

References

Acosta, V. T., Schildgen, T. F., Clarke, B. A., Scherler, D., Bookhagen, B., Wittmann, H., et al. (2015). Effect of vegetation cover on millennial-scale landscape denudation rates in east Africa. *Lithosphere*, *7*(4), 408–420.

Allen, S., Gruber, S., & Owens, I. (2009). Exploring steep bedrock permafrost and its relationship with recent slope failures in the southern alps of New Zealand. *Permafrost and Periglacial Processes*, *20*(4), 345–356.

Amidon, W. H., Bookhagen, B., Avouac, J.-P., Smith, T., & Rood, D. (2013). Late pleistocene glacial advances in the western Tibet interior. *Earth and Planetary Science Letters*, *381*, 210–221.

Anderson, R. S. (1998). Near-surface thermal profiles in alpine bedrock: Implications for the frost weathering of rock. *Arctic and Alpine Research*, *30*(4), 362–372.

Anderson, R. S., Anderson, S. P., & Tucker, G. E. (2013). Rock damage and regolith transport by frost: An example of climate modulation of the geomorphology of the critical zone. *Earth Surface Processes and Landforms*, *38*(3), 299–316.

Ben-Asher, M., Haviv, I., Roering, J. J., & Crouvi, O. (2017). The influence of climate and microclimate (aspect) on soil creep efficiency: Cinder cone morphology and evolution along the eastern Mediterranean Golan heights. *Earth Surface Processes and Landforms*, *42*(15), 2649–2662.

Boer, M., & Puigdefábregas, J. (2005). Effects of spatially structured vegetation patterns on hillslope erosion in a semiarid Mediterranean environment: a simulation study. *Earth Surface Processes and Landforms: The Journal of the British Geomorphological Research Group*, *30*(2), 149–167.

Chen, S.-A., Michaelides, K., Grieve, S. W., & Singer, M. B. (2019). Aridity is expressed in river topography globally. *Nature*, *573*(7775), 573–577.

Chevrier, V. F., & Rivera-Valentin, E. G. (2012). Formation of recurring slope lineae by liquid brines on present-day mars. *Geophysical Research Letters*, *39*(21), 21202. https://doi.org/10.1029/2012GL054119

Churchill, R. R. (1981). Aspect-related differences in Badlands slope morphology. *Annals of the Association of American Geographers*, *71*(3), 374–388.
Clark, M. K., Schoenbohm, L. M., Royden, L. H., Whipple, K. X., Burchfiel, B. C., Zhang, X., et al. (2004). Surface uplift, tectonics, and erosion of eastern Tibet from large-scale drainage patterns. *Tectonics*, *23*(1). https://doi/org/10.1029/2002TC001402
Clift, P. D., Wan, S., & Blusztajn, J. (2014). Reconstructing chemical weathering, physical erosion and monsoon intensity since 25 ma in the northern south China sea: A review of competing proxies. *Earth-Science Reviews*, *130*, 86–102.
Collins, D., & Bras, R. (2010). Climatic and ecological controls of equilibrium drainage density, relief, and channel concavity in dry lands. *Water Resources Research*, *46*(4).
Copernicus Climate Change Service (C3S). (2019). *C3S ERA5-land reanalysis*. Retrieved from https://cds.climate.copernicus.eu/
Costard, F., Forget, F., Mangold, N., & Peulvast, J. (2002). Formation of recent Martian debris flows by melting of near-surface ground ice at high obliquity. *Science*, *295*(5552), 110–113.
Crampton, C. (1977). A note on asymmetric valleys in the central Mackenzie river catchment, Canada. *Earth Surface Processes*, *2*(4), 427–429.
Delunel, R., Van Der Beek, P. A., Carcaillet, J., Bourlès, D. L., & Valla, P. G. (2010). Frost-cracking control on catchment denudation rates: Insights from in situ produced 10be concentrations in stream sediments (ecrins–pelvoux massif, French western alps). *Earth and Planetary Science Letters*, *293*(1–2), 72–83.
Desta, F., Colbert, J., Rentch, J. S., & Gottschalk, K. W. (2004). *Aspect induced differences in vegetation, soil, and microclimatic characteristics of an Appalachian watershed*. Castanea.
Didan, K. (2015). *Mod13a3 modis/terra vegetation indices monthly l3 global 1km sin grid v006. NASA EOSDIS land processes DAAC*. Retrieved from https://doi.org/10.5067/modis/mod13a3
Dietrich, W. E., & Perron, J. T. (2006). The search for a topographic signature of life. *Nature*, *439*(7075), 411.
Dimiceli, C., Carroll, M., Sohlberg, R., Kim, D., Kelly, M., & Townshend, J. (2015). Mod44b modis/terra vegetation continuous fields yearly l3 global 250 m sin grid v006. NASA EOSDIS land processes DAAC.
Diniega, S., Byrne, S., Bridges, N. T., Dundas, C. M., & McEwen, A. S. (2010). Seasonality of present-day Martian dune-gully activity. *Geology*, *38*(11), 1047–1050.
Dohrenwend, J. C. (1978). Systematic valley asymmetry in the central California coast ranges. *The Geological Society of America Bulletin*, *89*(6), 891–900.
Dunne, T. (1980). Formation and controls of channel networks. *Progress in Physical Geography*, *4*(2), 211–239.
Edwards, L. M., & Burney, J. (1987). *Soil erosion losses under freeze/thaw and winter ground cover using a laboratory rainfall simulator* (29). National Research Council, Division of Building Research.
Egholm, D., Nielsen, S., Pedersen, V. K., & Lesemann, J.-E. (2009). Glacial effects limiting mountain height. *Nature*, *460*(7257), 884–887.
Evans, I. S. (1977). World-wide variations in the direction and concentration of cirque and glacier aspects. *Geografiska Annaler: Series A, Physical Geography*, *59*(3–4), 151–175.
Evans, I. S., & Cox, N. J. (2005). Global variations of local asymmetry in glacier altitude: Separation of north–south and east–west components. *Journal of Glaciology*, *51*(174), 469–482.
Fitzgibbon, A., Pilu, M., & Fisher, R. B. (1996). Direct least square fitting of ellipses. *IEEE Transactions on Pattern Analysis and Machine Intelligence*, *21*(5), 476–480.
Gallardo-Cruz, J. A., Pérez-García, E. A., & Meave, J. A. (2009). β-diversity and vegetation structure as influenced by slope aspect and altitude in a seasonally dry tropical landscape. *Landscape Ecology*, *24*(4), 473–482.
Geroy, I., Gribb, M., Marshall, H.-P., Chandler, D., Benner, S. G., & McNamara, J. P. (2011). Aspect influences on soil water retention and storage. *Hydrological Processes*, *25*(25), 3836–3842.
Giorgi, F. (1988). Dry deposition velocities of atmospheric aerosols as inferred by applying a particle dry deposition parameterization to a general circulation model. *Tellus B: Chemical and Physical Meteorology*, *40*(1), 23–41.
Girona-Mata, M., Miles, E. S., Ragettli, S., & Pellicciotti, F. (2019). High-resolution snowline delineation from Landsat imagery to infer snow cover controls in a Himalayan catchment. *Water Resources Research*, *55*(8), 6754–6772. https://doi/org/10.1029/2019WR024935
Gupta, A. K., Yuvaraja, A., Prakasam, M., Clemens, S. C., & Velu, A. (2015). Evolution of the south Asian monsoon wind system since the late middle Miocene. *Palaeogeography, Palaeoclimatology, Palaeoecology*, *438*, 160–167.
Gutiérrez-Jurado, H. A., Vivoni, E. R., Cikoski, C., Harrison, J. B. J., Bras, R. L., & Istanbulluoglu, E. (2013). On the observed ecohydrologic dynamics of a semiarid basin with aspect-delimited ecosystems. *Water Resources Research*, *49*(12), 8263–8284. https://doi.org/10.1002/2013WR014364
Hales, T., & Roering, J. J. (2007). Climatic controls on frost cracking and implications for the evolution of bedrock landscapes. *Journal of Geophysical Research*, *112*(F2). https://doi.org/10.1029/2006JF000616
Hallet, B., Walder, J., & Stubbs, C. (1991). Weathering by segregation ice growth in microcracks at sustained subzero temperatures: Verification from an experimental study using acoustic emissions. *Permafrost and Periglacial Processes*, *2*(4), 283–300.
Hall, D., Riggs, G., & Salomonson, V. (2016). *Modis/terra snow cover daily l3 global 500 m grid, version 6*. Boulder, CO: NASA National Snow and Ice Data Center Distributed Active Archive Center.
Haselton, K., Hilley, G., & Strecker, M. R. (2002). Average pleistocene climatic patterns in the southern central andes: Controls on mountain glaciation and paleoclimate implications. *The Journal of Geology*, *110*(2), 211–226.
Haupt, H. F. (1967). Infiltration, overland flow, and soil movement on frozen and snow-covered plots. *Water Resources Research*, *3*(1), 145–161.
Head, J. W., Mustard, J. F., Kreslavsky, M. A., Milliken, R. E., & Marchant, D. R. (2003). Recent ice ages on mars. *Nature*, *426*(6968), 797.
Heimsath, A. M., DiBiase, R. A., & Whipple, K. X. (2012). Soil production limits and the transition to bedrock-dominated landscapes. *Nature Geoscience*, *5*(3), 210–214.
Heimsath, A. M., Dietrich, W. E., Nishiizumi, K., & Finkel, R. C. (2001). Stochastic processes of soil production and transport: Erosion rates, topographic variation and cosmogenic nuclides in the Oregon coast range. *Earth Surface Processes and Landforms: The Journal of the British Geomorphological Research Group*, *26*(5), 531–552.
Hershfield, D. M. (1974). The frequency of freeze-thaw cycles. *Journal of Applied Meteorology*, *13*(3), 348–354.
Holmgren, W. F., Hansen, C. W., & Mikofski, M. A. (2018). pvlib python: a python package for modeling solar energy systems. *Journal of Open Source Software*, *3*(29), 884. https://doi.org/10.21105/joss.00884
Hoylman, Z. H., Jencso, K. G., Hu, J., Martin, J. T., Holden, Z. A., Seielstad, C. A., &(2018). Hillslope topography mediates spatial patterns of ecosystem sensitivity to climate. *Journal of Geophysical Research: Biogeosciences*, *123*(2), 353–371. https://doi.org/10.1002/2017JG004108
Ielpi, A., & Lapôtre, M. G. (2020). A tenfold slowdown in river meander migration driven by plant life. *Nature Geoscience*, *13*(1), 82–86.

Inbar, A., Nyman, P., Rengers, F. K., Lane, P. N., & Sheridan, G. J. (2018). Climate dictates magnitude of asymmetry in soil depth and hillslope gradient. *Geophysical Research Letters*, *45*(13), 6514–6522.
Istanbulluoglu, E., & Bras, R. L. (2005). Vegetation-modulated landscape evolution: Effects of vegetation on landscape processes, drainage density, and topography. *Journal of Geophysical Research*, *110*(F2).
Istanbulluoglu, E., Yetemen, O., Vivoni, E. R., Gutiérrez-Jurado, H. A., & Bras, R. L. (2008). Eco-geomorphic implications of hillslope aspect: Inferences from analysis of landscape morphology in central New Mexico. *Geophysical Research Letters*, *35*(14). 10.1029/2018GL077629
Iwata, Y., Nemoto, M., Hasegawa, S., Yanai, Y., Kuwao, K., & Hirota, T. (2011). Influence of rain, air temperature, and snow cover on subsequent spring-snowmelt infiltration into thin frozen soil layer in northern Japan. *Journal of Hydrology*, *401*(3–4), 165–176.
Johnstone, S. A., Chadwick, K. D., Frias, M., Tagliaro, G., & Hilley, G. E. (2017). Soil development over mud-rich rocks produces landscape-scale erosional instabilities in the northern gabilan mesa, California. *Bulletin*, *129*(9–10), 1266–1279.
Johnstone, S. A., Finnegan, N. J., & Hilley, G. E. (2017). Weak bedrock allows north-south elongation of channels in semi-arid landscapes. *Earth and Planetary Science Letters*, *478*, 150–158.
Johnstone, S. A., & Hilley, G. E. (2015). Lithologic control on the form of soil-mantled hillslopes. *Geology*, *43*(1), 83–86.
JPL, N. (2013). *Nasa shuttle radar topography mission global 1 arc second*. https://doi.org/10.5067/MEaSUREs/SRTM/SRTMGL1.003
Kane, P. (1978). Origins of valley asymmetry at Sarah canyon, California. *Yearbook of the Association of Pacific Coast Geographers*, *40*, 103–115.
Kang, S., Kim, S., Oh, S., & Lee, D. (2000). Predicting spatial and temporal patterns of soil temperature based on topography, surface cover and air temperature. *Forest Ecology and Management*, *136*(1–3), 173–184.
Kidron, G. J., Kronenfeld, R., & Starinsky, A. (2016). Wind as a cooling agent: substrate temperatures are responsible for variable lithobiont-induced weathering patterns on west-and east-facing limestone bedrock of the Negev. *Earth Surface Processes and Landforms*, *41*(14), 2078–2084.
Kirby, E., & Whipple, K. (2001). Quantifying differential rock-uplift rates via stream profile analysis. *Geology*, *29*(5), 415–418.
Klucher, T. M. (1979). Evaluation of models to predict insolation on tilted surfaces. *Solar Energy*, *23*(2), 111–114.
Kreslavsky, M., & Head, J. (2003). North–south topographic slope asymmetry on mars: Evidence for insolation-related erosion at high obliquity. *Geophysical Research Letters*, *30*(15). https://doi.org/10.1029/2003GL017795
Kumar, L., Skidmore, A. K., & Knowles, E. (1997). Modelling topographic variation in solar radiation in a GIS environment. *International Journal of Geographical Information Science*, *11*(5), 475–497.
Lebedeva, M. I., & Brantley, S. L. (2013). Exploring geochemical controls on weathering and erosion of convex hillslopes: Beyond the empirical regolith production function. *Earth Surface Processes and Landforms*, *38*(15), 1793–1807.
Ma, L., Chabaux, F., West, N., Kirby, E., Jin, L., & Brantley, S. (2013). Regolith production and transport in the Susquehanna shale hills critical zone observatory, part 1: Insights from u-series isotopes. *Journal of Geophysical Research: Earth Surface*, *118*(2), 722–740. https://doi.org/10.1002/jgrf.20037
Marshall, J. A., Roering, J. J., Bartlein, P. J., Gavin, D. G., Granger, D. E., Rempel, A. W., et al. (2015). Frost for the trees: Did climate increase erosion in unglaciated landscapes during the late pleistocene?. *Science advances*, *1*(10), e1500715.
Marston, R. A. (2010). Geomorphology and vegetation on hillslopes: Interactions, dependencies, and feedback loops. *Geomorphology*, *116*(3–4), 206–217.
Martone, M., Rizzoli, P., Wecklich, C., González, C., Bueso-Bello, J.-L., Valdo, P., et al. (2018). The global forest/non-forest map from tandem-x interferometric SAR data. *Remote Sensing of Environment*, *205*, 352–373.
Matsuoka, N. (1990). The rate of bedrock weathering by frost action: field measurements and a predictive model. *Earth Surface Processes and Landforms*, *15*(1), 73–90.
Matsuoka, N., & Murton, J. (2008). Frost weathering: Recent advances and future directions. *Permafrost and Periglacial Processes*, *19*(2), 195–210.
McGuire, L. A., Pelletier, J. D., & Roering, J. J. (2014). Development of topographic asymmetry: Insights from dated cinder cones in the western United States. *Journal of Geophysical Research: Earth Surface*, *119*(8), 1725–1750. https://doi.org/10.1002/2014JF003081
Melton, M. A. (1960). Intravalley variation in slope angles related to microclimate and erosional environment. *The Geological Society of America Bulletin*, *71*(2), 133–144.
Middleton, N., & Thomas, D. (1997). *World atlas of desertification* (pp. 171–180). UNEP. Retrieved from http://digitallibrary.un.org/record/245955
Murton, J. B., Peterson, R., & Ozouf, J.-C. (2006). Bedrock fracture by ice segregation in cold regions. *Science*, *314*(5802), 1127–1129.
Naylor, S., & Gabet, E. J. (2007). Valley asymmetry and glacial versus nonglacial erosion in the bitterroot range, Montana, USA. *Geology*, *35*(4), 375–378.
Ojha, L., McEwen, A., Dundas, C., Byrne, S., Mattson, S., Wray, J., &(2014). Hirise observations of recurring slope lineae (RSL) during southern summer on Mars. *Icarus*, *231*, 365–376.
Olen, S. M., Bookhagen, B., & Strecker, M. R. (2016). Role of climate and vegetation density in modulating denudation rates in the Himalaya. *Earth and Planetary Science Letters*, *445*, 57–67.
Page, D. P. (2007). Recent low-latitude freeze–thaw on mars. *Icarus*, *189*(1), 83–117.
Parsons, A. J. (1988). *Hillslope form*. Routledge.
Pelletier, J. D., Barron-Gafford, G. A., Gutiérrez-Jurado, H., Hinckley, E.-L. S., Istanbulluoglu, E., McGuire, L. A., et al. (2018). Which way do you lean? using slope aspect variations to understand critical zone processes and feedbacks. *Earth Surface Processes and Landforms*, *43*(5), 1133–1154.
Pelletier, J. D., McGuire, L. A., Ash, J. L., Engelder, T. M., Hill, L. E., Leroy, K. W., et al. (2011). Calibration and testing of upland hillslope evolution models in a dated landscape: Banco Bonito, New Mexico. *Journal of Geophysical Research: Earth Surface*, *116*(F4). https://doi.org/10.1029/2011JF001976
Pelletier, J. D., & Swetnam, T. L. (2017). Asymmetry of weathering-limited hillslopes: the importance of diurnal covariation in solar insolation and temperature. *Earth Surface Processes and Landforms*, *42*(9), 1408–1418.
Perron, J. T., Kirchner, J. W., & Dietrich, W. E. (2009). Formation of evenly spaced ridges and valleys. *Nature*, *460*(7254), 502–505.
Pierce, K. L., & Colman, S. M. (1986). Effect of height and orientation (microclimate) on geomorphic degradation rates and processes, late-glacial terrace scarps in central Idaho. *The Geological Society of America Bulletin*, *97*(7), 869–885.
Poulos, M. J., Pierce, J. L., Flores, A. N., & Benner, S. G. (2012). Hillslope asymmetry maps reveal widespread, multi-scale organization. *Geophysical Research Letters*, *39*(6). https://doi.org/10.1029/2012GL051283
Rasmussen, C., McGuire, L., Dhakal, P., & Pelletier, J. D. (2017). Coevolution of soil and topography across a semiarid cinder cone chronosequence. *Catena*, *156*, 338–352.

Rempel, A. W., Marshall, J. A., & Roering, J. J. (2016). Modeling relative frost weathering rates at geomorphic scales. *Earth and Planetary Science Letters*, *453*, 87–95.

Richardson, P., Perron, J., Miller, S., & Kirchner, J. (2020a). Modeling the formation of topographic asymmetry by aspect-dependent erosional processes and lateral channel migration. *Journal of Geophysical Research: Earth Surface*, *125*(7), e2019JF005377. https://doi.org/10.1029/2019JF005377

Richardson, P., Perron, J., Miller, S., & Kirchner, J. (2020b). Unraveling the mysteries of asymmetric topography at gabilan mesa, California. *Journal of Geophysical Research: Earth Surface*, *125*(7), e2019JF005378. https://doi.org/10.1029/2019JF005378

Richardson, P., Perron, J. T., & Schurr, N. (2019). Influences of climate and life on hillslope sediment transport. *Geology*, *47*(5), 423–426.

Rubanenko, L., Venkatraman, J., & Paige, D. A. (2019). Thick ice deposits in shallow simple craters on the moon and mercury. *Nature Geoscience*, *1*.

Running, S., Mu, Q., & Zhao, M. (2017). Mod16a2 modis/terra net evapotranspiration 8-day l4 global 500m sin grid v006. NASA EOSDIS Land Processes DAAC.

Scherler, D. (2014). Climatic limits to headwall retreat in the Khumbu Himalaya, eastern Nepal. *Geology*, *42*(11), 1019–1022.

Sexton, J. O., Song, X.-P., Feng, M., Noojipady, P., Anand, A., Huang, C., &(2013). Global, 30-m resolution continuous fields of tree cover: Landsat-based rescaling of Modis vegetation continuous fields with Lidar-based estimates of error. *International Journal of Digital Earth*, *6*(5), 427–448.

Sinha, T., & Cherkauer, K. A. (2008). Time series analysis of soil freeze and thaw processes in Indiana. *Journal of Hydrometeorology*, *9*(5), 936–950.

Smith, B. (1978). Aspect-related variations in slope angle near béni abbès, western Algeria. *Geografiska Annaler: Series A, Physical Geography*, *60*(3–4), 175–180.

Smith, T. (2020). Hillslope asymmetry: Initial release (version v1.0.0). Zenodo. https://doi.org/10.5281/zenodo.3839251

Smith, T., Rheinwalt, A., & Bookhagen, B. (2019). Determining the optimal grid resolution for topographic analysis on an airborne Lidar dataset. *Earth Surface Dynamics*, *7*(2), 475–489. Retrieved from https://www.earth-surf-dynam.net/7/475/2019/ https://doi/org/10.5194/esurf-7-475-2019

Smith, D., Zuber, M., Neumann, G., Guinness, E., & Slavney, S. (2003). Mars *global surveyor laser altimeter mission experiment gridded data record*. Nasa planetary data system (Tech. Rep.). MGS-M-MOLA-5-MEGDR-L3-V1. 0.

Snyder, N. P., Whipple, K. X., Tucker, G. E., & Merritts, D. J. (2000). Landscape response to tectonic forcing: Digital elevation model analysis of stream profiles in the Mendocino triple junction region, northern California. *The Geological Society of America Bulletin*, *112*(8), 1250–1263.

Starkloff, T., Hessel, R., Stolte, J., & Ritsema, C. (2017). Catchment hydrology during winter and spring and the link to soil erosion: A case study in Norway. *Hydrology*, *4*(1), 15.

Sternberg, M., & Shoshany, M. (2001). Influence of slope aspect on Mediterranean woody formations: Comparison of a semiarid and an arid site in Israel. *Ecological Research*, *16*(2), 335–345.

Tarboton, D. G., Bras, R. L., & Rodriguez-Iturbe, I. (1991). On the extraction of channel networks from digital elevation data. *Hydrological Processes*, *5*(1), 81–100.

Trabucco, A., & Zomer, R. (2019). *Global aridity index and potential evapotranspiration (et0) climate database v2*. https://doi/org/10.6084/m9.figshare.7504448,v3

van Breda Weaver, A. (1991). The distribution of soil erosion as a function of slope aspect and parent material in Ciskei, southern Africa. *Geojournal*, *23*(1), 29–34.

Wan, Z., Hook, S., & Hulley, G. (2015). *Mod11a1 modis/terra land surface temperature*. Emissivity Daily L3 Global 1 km SIN Grid.

West, N., Kirby, E., Bierman, P., & Clarke, B. A. (2014). Aspect-dependent variations in regolith creep revealed by meteoric 10be. *Geology*, *42*(6), 507–510.

Whipple, K. X., Forte, A. M., DiBiase, R. A., Gasparini, N. M., & Ouimet, W. B. (2017). Timescales of landscape response to divide migration and drainage capture: Implications for the role of divide mobility in landscape evolution. *Journal of Geophysical Research: Earth Surface*, *122*(1), 248–273. https://doi/org/10.1002/2016JF003973

Yamazaki, D., Ikeshima, D., Sosa, J., Bates, P. D., Allen, G., & Pavelsky, T. (2019). Merit hydro: A high-resolution global hydrography map based on latest topography datasets. *Water Resources Research*, *55*(6), 5053–5073. https://doi.org/10.1029/2019WR024873

Yamazaki, D., Ikeshima, D., Tawatari, R., Yamaguchi, T., O'Loughlin, F., Neal, J. C., et al. (2017). A high-accuracy map of global terrain elevations. *Geophysical Research Letters*, *44*(11), 5844–5853. https://doi/org/10.1002/2017GL072874

Yetemen, O., Istanbulluoglu, E., & Duvall, A. R. (2015). Solar radiation as a global driver of hillslope asymmetry: Insights from an ecogeomorphic landscape evolution model. *Water Resources Research*, *51*(12), 9843–9861. https://doi.org/10.1002/2015WR017103

Yetemen, O., Istanbulluoglu, E., & Vivoni, E. R. (2010). The implications of geology, soils, and vegetation on landscape morphology: Inferences from semi-arid basins with complex vegetation patterns in central New Mexico, USA. *Geomorphology*, *116*(3–4), 246–263.

Zomer, R. J., Trabucco, A., Bossio, D. A., & Verchot, L. V. (2008). Climate change mitigation: A spatial analysis of global land suitability for clean development mechanism afforestation and reforestation. *Agriculture, Ecosystems & Environment*, *126*(1–2), 67–80.